Title

Computational Study of an Iron(II) Polypyridine Electrocatalyst for CO2 Reduction: Key Roles for Intramolecular Interactions in CO2 Binding and Proton Transfer

Journal

Inorganic Chemistry, 59(12)

ISSN

0020-1669

Authors

Loipersberger, Matthias
Zee, David Z
Panetier, Julien A
et al.

Publication Date

2020-06-15

DOI

10.1021/acs.inorgchem.0c00454

Computational Study of an Iron(II)-Polypyridine Electrocatalyst for CO_2 Reduction: Key Roles for Intramolecular Interactions in CO_2 Binding and Proton Transfer

Matthias Loipersberger,[†,‡] David Z. Zee,[¶,‡] Julien A. Panetier,[§,‡] Christopher J. Chang,[¶,∥,⊥] Jeffrey R. Long,[¶,#,@] and Martin Head-Gordon[*,†,∥]

†*Pitzer Center for Theoretical Chemistry, Department of Chemistry, University of California, Berkeley, California 94720, USA*

‡*Joint Center for Artificial Photosynthesis, Lawrence Berkeley National Laboratory, Berkeley, California 94720, USA*

¶*Department of Chemistry, University of California, Berkeley, California 94720, USA*

§*Department of Chemistry, State University of New York at Binghamton, Binghamton, New York, 13902, USA*

∥*Chemical Sciences Division, Lawrence Berkeley National Laboratory, Berkeley*

⊥*Department of Molecular and Cell Biology University of California Berkeley*

#*Materials Sciences Division, Lawrence Berkeley National Laboratory, Berkeley*

@*Department of Chemical & Biomolecular Engineering, University of California Berkeley*

E-mail: mhg@cchem.berkeley.edu

Abstract

A solar-driven conversion of CO_2 into fuels by artificial photosynthesis would not only mitigate the greenhouse effect but also provide an alternative to obtain fuels in a renewable fashion. To this end, the new iron polypyridine catalyst $[Fe(bpy^{NHEt}PY2)L_2]^{2+}$ ($L = H_2O$, CH_3CN) was recently developed for the electrochemical reduction of CO_2 to CO. In this study, we performed density functional theory (DFT) electronic structure calculations to shed light on a possible pathway for CO_2 reduction and the origin of the selectivity between CO_2 versus hydrogen evolution reaction.

The metal center remains Lewis acidic throughout the reduction process due to ligand loss and mainly ligand based reduction stabilized by antiferromagnetic coupling to a high spin Fe(II) center. This results in a high barrier for hydride formation but a facile addition and activation of CO_2 via an η^2 coordination and stabilizing hydrogen bonding by the amine group. The second unoccupied equatorial coordination site opens up the possibility for an intramolecular protonation with a coordinated water ligand. This facilitates protonation because not only CO_2 but also the proton source H_2O is activated and properly aligned for a proton transfer due to the $Fe-OH_2$ bond; consequently, both protonation steps are facile. The moderate ligand field allows a rapid ligand exchange for a second intramolecular protonation step and facilitates an exergonic CO release. The lower selectivity of the related $[Fe(bpy^{OH}PY2)L_2]^{2+}$ compound can be related to the more acidic second coordination sphere because it opens up the possibility of an intramolecular proton transfer which has a comparable barrier to CO_2 addition.

Introduction

The world energy consumption is approaching a record high 15000 Mtoe. Fossil fuels are still one of the main energy sources resulting in a continuous rise of CO_2 emissions.[1] This anthropogenic emission yields unprecedented high concentration of CO_2 in the atmosphere which is one of the main driving forces of global climate change. This has focused considerable attention on artificial photosynthesis.[2,3] The solar driven conversion of CO_2 into fuels

or other chemically useful compounds, will not only mitigate the greenhouse effect but also provide a valuable method to obtain fuels in a renewable fashion. The inertness of CO_2 is illustrated by the negative one-electron reduction potential; however, coupled multi-electron and multi-proton reductions make an efficient conversion at modest potentials feasible. Unfortunately, these potentials are similar to the potential of the hydrogen evolution reaction (see Table 1).[4] This means that its reduction requires not only energy but also the deployment of a catalyst which is ideally substrate selective, efficient, stable and made out of earth abundant materials. Several strategies are known for efficient CO_2 conversion such as biological,[5] hydrogenation,[6] photochemical,[7] electrochemical,[8] or photoelectrochemical reduction.[4,9,10] Among possible products CO is one of the most economically viable.[11] It can be further utilized to synthesize fuels using the Fischer-Tropsch process.[12]

One approach to reduce CO_2 is to employ heterogeneous catalysts such as earth abundant metallic electrodes; however, the catalytic mechanisms can be difficult to study, and catalytic activities often suffer from poisoning of the electrode by the intermediates and substrate selectivity.[4,10,13–16] Indeed only Cu is capable of reducing CO_2 beyond CO to C1 or C2 hydrocarbons, and not selectively or with high energy efficiency.[17]

As an alternative strategy, molecular homogeneous electrocatalysts can show high selectivity, good turnover numbers, and fast catalytic rates. However, they usually operate at a high overpotential. When operated in aqueous media, proton reduction takes place at a similar potential (see table 1); thus, a high selectivity for the CO_2 reduction reaction (CO2RR) over the hydrogen evolution reaction (HER) is especially desirable. The catalyst acts as an electron shuttle between an electrode and CO_2 in solution. It accepts electrons and stabilizes intermediates to facilitate the transformation which results in a smaller overpotential and faster turnover rates. Many different molecular catalysts have been developed but are often based on expensive metals like Re, Ir or Ru.[4,8] However, many notable catalysts containing earth abundant first row transition metals such as Mn, Co, Fe, Ni, Cu and Zn were developed recently.[18–25] They can be incorporated into covalent or metal organic frameworks,[26–28]

attached on surfaces[29,30] or incorporated into a flow cell architecture[31] to further enhance their activity.

Table 1: Reduction potentials of CO_2 and proton reduction at pH = 7 versus NHE.[4,32]

$2\,H^+ + 2e^-$	$\longrightarrow$	H_2	$E^0 = -0.42$ V
$CO_2 + 2\,H^+ + 2\,e^-$	$\longrightarrow$	$CO + H_2O$	$E^0 = -0.53$ V
$CO_2 + e^-$	$\longrightarrow$	$CO_2^{\bullet -}$	$E^0 = -1.90$ V

In the quest for rational catalyst design, mechanistic studies of both a spectroscopic and computational nature are essential to uncover possible intermediates and intrinsic factors influencing selectivity and activity. Several molecular electrocatalysts for the two electron, two proton reduction of CO_2 to CO were studied thoroughly; most prominently, the $Re(bpy)(CO)_3Cl$ family and its derivatives. Experimental efforts include (spectro) electrochemical analysis, rapid scan Fourier-transform infrared spectroscopy (FTIR) spectroscopy during stopped-flow mixing, kinetic isotope studies and X-ray absorption spectroscopy.[33–40] In addition, a mechanism was proposed using density functional theory (DFT) calculations.[41] Further computational studies elucidated the mechanistic differences between the rhenium and manganese derivatives and explained the importance of weak Brønsted acids for the manganese catalyst.[42,43] The second protonation was determined to be the rate limiting step which coincides with the proton dependence of the catalytic activity. The high selectivity favoring CO_2 reduction over HER is one of the main advantages of this family of catalysts. Although thermodynamics favors the formation of a hydride intermediate, the high reaction barrier compared to the essentially barrierless CO_2 addition makes the H_2 pathway kinetically inaccessible.

Another well-studied system is $[Ni(cyclam)]^{2+}$ (cyclam = 1,4,8,11-tetraazacyclotetradecane), which was also investigated using DFT.[44,45] A single initial reduction of the metal, followed by CO_2 binding is proposed. Next, a proton coupled electron transfer (PCET) step yields a carboxylate anion followed by the concerted second protonation and C–O bond cleavage to yield CO and H_2O. The dissociation of CO then regenerates the catalyst to close the cat-

alytic cycle. The Ni(II)-CO species can also accept an electron and the calculated reduction potentials are much lower than for the initial reduction of the Ni(II) complex. Dissociation of CO from the reduced Ni(I)-CO species is an endergonic process. Therefore, this species was predicted to accumulate during catalysis.[45] This poisoning of the catalyst is also observed experimentally and determined to be rate-limiting.[46,47]

Iron is one of the most earth-abundant elements. Hence, it is especially desirable to use it as the central metal of a catalyst. The prominent catalyst family for the conversion of CO_2 to CO are iron porphyrin-based. They show very high turnover rates accompanied by a high selectivity for CO_2 reduction.[22,48] The catalytic pathway for the iron tetraphenylporphyrin starts with two initial reductions of the catalyst, a recent combined spectroscopic and computational investigation revealed that both reductions are mainly ligand-centered.[49] This is followed by the formation of a CO_2 adduct, a two step protonation and dehydration. At low acid concentrations, the second protonation is the rate-limiting step. The CO release to regenerate the catalyst is coupled to another reduction.[50,51] A computational study confirmed that the second protonation has a significantly higher barrier than the first protonation.[52] Further mechanistic studies clarified the role of the pendant phenol groups in the more active heme catalyst: the CO_2 adduct is initially stabilized by the pendant phenol groups through intramolecular hydrogen bonding. The first protonation of the CO_2 adduct is believed to involve proton transfer from the pendant phenol group, followed by reprotonation of the phenoxide ion by external phenol. Thus, the pre-positioned phenol groups act as both hydrogen bonding stabilizers and as local proton donors[53] The second protonation is assumed to occur via a PCET step with concerted cleavage of the C−O bond.[53,54]

The incorporation of proton relays like phenol groups in the secondary and outer coordination spheres is a well-established strategy in bioinspired catalyst design to control product selectivity and enhance catalytic activity.[20,22,48,55–62] Correct positioning of the hydrogen bonding moiety can play crucial role in tuning the activity of the catalyst for CO_2 to CO reduction.[63,64] To this end, a recent experimental study identified a family of non-heme iron

complexes $[Fe(bpy^{R}PY2\,Me)]^{2+}$ with various protic functional groups in the second coordination sphere as a viable catalysts for the conversion of CO_2 to CO in acetonitrile solutions with 11 M H_2O.[64] Among the tested compositions, the ethylamine functional group (R = NHEt) is notable for affording the $[Fe(bpy^{NHEt}PY2\,Me)L_2]^{2+}$ complex with high CO_2 to CO conversion activity, high selectivity against HER, and electrolytically stable for 12 h (see figure 1). Interestingly, the Fe complex bearing the more acidic hydroxyl group instead favors production of H_2 CO in a *ca.* 2:1 ratio.[64] The new catalyst features three functional partitions: a reactive metal center, a ligand-based electron reservoir, and a secondary coordination sphere Brønsted-acidic moiety. However, the mechanistic details remain unclear. This study presents first efforts to elucidate the Fe-catalyzed CO_2 reduction mechanism using electronic structure calculations.

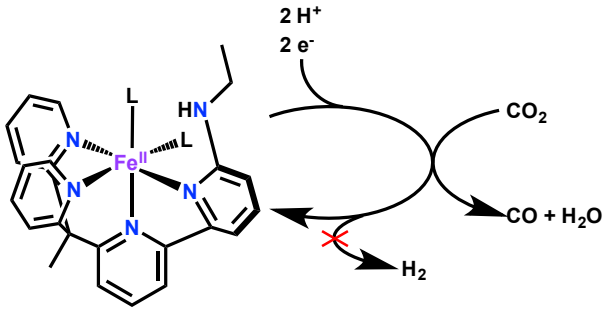

Figure 1: The catalytic system $[Fe(bpy^{NHEt}PY2\,Me)L_2]^{2+}$ (L = CH_3CN), a CO_2 reduction catalyst with high selectivity against hydrogen evolution reaction.

Computational Model

Density functional theory calculations were performed with the Q-Chem package[65] (version 5.0.2) using the ωB97X-D[66] and ωB97M-V[67] functionals. All reported geometries were fully optimized in the gas phase without constraints. Minimum and transition state structures were verified by having only positive, real frequency eigenvalues or having only one imaginary frequency, respectively. The geometry optimization and frequency calculations were performed with ωB97X-D and a mixed basis (def2-SVP basis for all main group elements, def2-TZVP basis set for Fe).[68] Single point calculations with the larger def2-TZVPP basis[68] using ωB97M-V[67] were used to refine the electronic structure for free energies and barrier heights. The ωB97M-V functional has performed very well in comparative assessments of density functionals for both main group[69] and transition metal[70] chemistry. The solvation energies were calculated using the C-PCM model (acetonitrile, $\epsilon = 37.5$) as implemented in Q-Chem.[71] Additional calculation were performed with B97-D[72] and B3LYP[73–75]+D3[76] to gauge functional dependency and can be found in the Supporting Information (SI). CASSCF/NEVPT2 calculations were performed with Orca (version 4.0.0.2)[77] employing the RI approximation along with the def2-TZVPP basis and auxiliary basis set.[78] All molecular orbitals (MO) were plotted using an isovalue of 0.03 (blue: positive, red: negative values) and spin density using an isovalue of 0.005 (green: α spin density, yellow: β spin density).

The reaction free energies ($\Delta_R G$), activation energies ($\Delta G^{\ddagger}$), reduction potentials and pK_{a} values were calculated based on the standard thermodynamic cycles (see Refs[41,45,79,80]). The Gibbs free energies include enthalpic contributions from the zero-point energy correction and the entropic contribution is calculated from the vibrational frequencies at T = 298 K. Solvation energies were approximated by performing single point calculations applying the implicit C-PCM solvent model.

The calculation of pK_{a} values requires the Gibbs free energy of a proton, which cannot be calculated using quantum chemical methods. Therefore, we used the experimental value based on the Sackur-Tetrode equation and an estimated solvation energy of $G(\mathrm{H}^+) = -264.6$ kcal/mol.[79,81]

Employing this experimental value makes it challenging to compute accurate pK_a values because an error of 1.36 kcal/mol leads to a deviation of 1 pK_a unit.[82] Other studies found deviations between this approach and experimental values of ± 3 units.[83] In this vein, we tested our computational protocol with two acids (CH_3COOH and phenol); in both cases the computed pK_a values were lower than the experimental ones in acetonitrile by 4 units (see SI table S10). In spite of this systematic computational error, calculated relative pK_a values are more reliable because of favorable error cancellation by removing the experimental free energy of the proton. Thus, calculated pK_a values should mainly be compared against each other. Furthermore, it is important to note that electrolyses with the Fe catalysts were conducted in a solution of 11 M H_2O in acetonitrile, saturated with 1 atm of CO_2, not in pure acetonitrile.[64] These experimental conditions lead to several important complications that merit further discussion here. First, experimental pK_a values of acids in mixtures of acetonitrile and water are lower than in pure acetonitrile.[84,85] This decrease in pKa is not accounted for by the implicit solvent model used in our calculations. Therefore, the actual pK_a of possible intermediates under the experimental conditions should be lower than the calculated values. An overview of pK_a values and corresponding free energies for all relevant intermediates are provided in table S11. Second, the introduction of CO_2 to the water-acetonitrile mixture lowers the effective pKa of H_2O to 11.2.[86] This occurs via the complexation between CO_2 and OH^-, and is not accounted for in our computational model either.

Reduction potentials are reported against the ferrocene/ferrocenium (Fc/Fc^+) couple used as an internal standard.[80,87] This method allows accurate predictions even at a modest level of theory with an accuracy of < 100 mV relative to experimental values.[80] However, other studies have shown that the errors can be larger for charged transition metal complexes and are functional-dependent. [83,88–90]

The correct prediction of (adiabatic) spin gaps ($\Delta_{hs/ls}G = G(hs) - G(ls)$) in first row TS metal complexes is very sensitive to the choice of the density functional. Generalized gradient

approximation (GGA) functionals tent to overstabilize the low-spin (ls) state whereas hybrid functionals tend to overstabilize the high-spin (hs) state. The amount of Hartree-Fock (HF) exchange plays a crucial role because it is found that spin gaps depend almost linearly on the amount of HF exchange incorporated in the functional. An increasing amount of HF exchange stabilizes the hs state.[91–94] Various studies specifically for iron complexes revealed that hybrid functionals perform better for correctly predicting the ground spin state. However, the recommended amount of HF exchange varies.[92,94–96] The range separated hybrid ωB97M-V (short range: 12% HF exchange) performed best in predicting both the experimentally known spin gap of $[Fe(bpy^{NHEt}PY2\,Me)L_2]^{2+}$ (L = CH_3CN) and the reduction potentials (see SI).

$[Fe(bpy^{NHEt}PY2\,Me)L_2]^{2+}$ has two open coordination sites, which are occupied by solvent ligands. Acetonitrile, water, or hydroxide ion are conceivable due to the experimental conditions. All three ligands occupy similar positions in the spectrochemical series. However, water not only interacts as a ligand but can also form intramolecular hydrogen bonds. This can lead to an overestimation of the dissociation energies, as hydrogen bonding might in the experiment be provided by solvent (water) molecules. The hydroxide ion is charged which results in overestimation of the binding energy to positively charged species because solvation is only taken into account implicitly. Acetonitrile solely acts as a σ-donating ligand and is not charged. Hence, it is used as the primary ligand in this study to compare the stability of different coordination numbers.

We reasoned that H_2O should be used as the main proton source for calculating reaction barriers (i.e. kinetics) involving protonation reactions, because under the experimental conditions the concentration of water is significantly higher (by a factor of roughly 10^5) than both H_3O^+ and H_2CO_3.[45] The reaction barriers with H_2CO_3 are also presented. These kinetic barriers do not reflect the experimental catalytic system (as the concentration of carbonic acid is vanishingly small). We include them here to illustrate how barriers for the protonation steps can vary when using a stronger acid source; for example, when another acid

is added to the reaction mixture. The calculated pK_a of H_2CO_3 is significantly lower than commonly used acids sources like phenol[97] or trifluoroethanol[18] (see table S10). Therefore, the H_2CO_3 barriers should be lower than with these weaker acids.

Results and Discussion

Various reaction pathways for the catalytic reaction of $[Fe(bpy^{NHEt}PY2\,Me)L_2)]^{2+}$ are explored in this study using electronic structure calculations. The proposed reaction mechanism is depicted in figure 2. The paper is structured as follows: in the first part, the catalytic cycle is described step-wise starting with the initial reduction, followed by CO_2 fixation and protonation. In the second part, alternative intermediates are presented and discussed with respect to their relevance.

A consistent naming scheme is used throughout the manuscript which encodes the multiplicity (2S+1), the total charge, the iron coordination number (CN) and a consecutive number X for each intermediate step (1: initial complex, 2: CO_2 adduct, ...): $^{\mathbf{multiplicity}}_{\mathbf{charge}}\mathbf{X}^{\mathbf{CN}}$, e.g. $^5_2\mathbf{1}^6$ describes the initial hexacoordinated complex $[Fe(bpy^{NHEt}PY2\,Me)L_2)]^{2+}$ in the quintet spin state and overall charge 2+.

Reduction of the Initial Complex

The optimized geometry of the initial complex is illustrated in figure 3. The calculated and experimentally determined X-ray crystal structure show good agreement between theory and experiment using the ωB97X-D functional (see SI table S1). The Fe(II) compound shows a distorted octahedral coordination by a tetradentate chelating ligand ($bpy^{NHEt}PY2\,Me$) and two solvent molecules (in this case, acetonitrile) (figure 3 (a)). The spin gap between high and low-spin states is only 1.5 kcal/mol with the low-spin state being higher in energy. This is in good agreement with the experimentally determined effective magnetic moment μ_{eff}=1.4 μ_B,[64] which demonstrates the presence of both spin states in experimental samples and a spin gap of less than 1.0 kcal/mol.

The cyclic voltammetry (CV) of $[Fe(bpy^{NHEt}PY2\,Me)L_2)]^{2+}$ exhibits two one-electron reduction events within a narrow 0.2 V window at −1.79 V and −1.87 V versus Fc/Fc^+.[64] The calculated reduction potential of $[Fe(bpy^{NHEt}PY2\,Me)L_2)]^{2+}$, here denoted $^5_2\mathbf{1}^6$, to yield

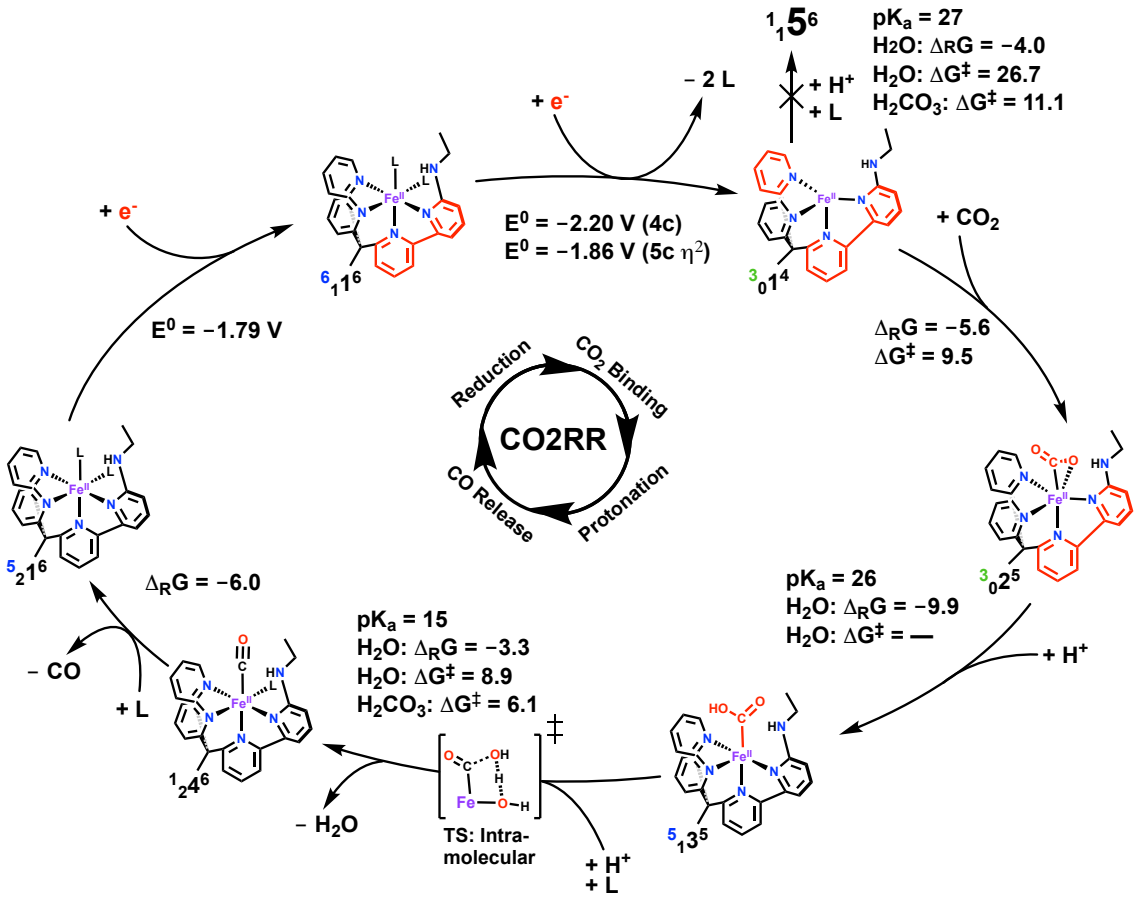

Figure 2: Proposed mechanism for the selective CO_2 to CO reduction using $[Fe(bpy^{NHEt}PY2\,Me)L_2)]^{2+}$. The red colored molecular moiety indicate localization of the excess electrons; reaction and activation energies in kcal/mol; reduction potentials against Fc/Fc^+; L = CH_3CN expect for the free energies and activation energies of the intramolecular protonation steps where water/hydroxide is used (see main text for justification); pK_a values were computed using L = CH_3CN.

$[Fe(bpy^{NHEt}PY2\,Me)L_2)]^+$, $^{6}_{1}1^{6}$, is −1.79 V, in excellent agreement with the experimental result; the analysis of the spin densities of the unreduced complex $^{5}_{2}1^{6}$ versus the one electron reduced complex $^{6}_{1}1^{6}$ in figures 3 (b) and (c) reveals a non-innocent ligand-based reduction in the bpy π^*. A ligand-based reduction was also observed in all other spin states and is robust to the choice of DFT functional. A schematic MO diagram is depicted in figure 4 (a).

The second reduction event is accompanied by the dissociation of one or two solvent ligands. We identified two possible intermediates: the four-coordinate trigonal pyramidal complex ($[Fe(bpy^{NHEt}PY2\,Me)]^0$, $^{3}_{0}1^{4}$) and the five-coordinate trigonal bipyramidal species

([Fe(bpy$^{\mathrm{NHEt}}$PY2Me)(η^2−NCCH$_3$)]^0, $^3_0$1^4), see figure 5. The ground states for both complexes $^3_0$1^4 and $^3_0$1^5 were calculated to be triplet states, with the corresponding quintet states calculated to be 4.5 and 1.9 kcal/mol higher in energy, respectively.

The complex $^3_0$1^5 contains a side-on bound, bent acetonitrile ligand ($\angle(NCC) = 142.4°$), which implies a ligand-based second reduction step featuring a reduced acetonitrile in an η^2 coordination mode. Although rare, the side-on bound η^2 acetonitrile ligand has been crystallographically observed in a number of low valent transition metal complexes, including Mo,[98] W,[99] Ni,[100] Ir,[101] and Nb.[102] The spin density plot and the β HOMO and β HOMO−1 shed light on the electronic structure: two β electrons in an acetonitrile π^* orbital and a bpy π^* orbital couple antiferromagnetically (afm) with the Fe-t$_{2g}$ orbitals of a high spin metal center to an overall triplet state (see fig. S1 (a) & (b)). In addition, the decrease in the coordination number and η^2 coordination of CH$_3$CN results in a distorted ligand field. The schematic MO diagram in figure 4 (b) summarizes the electronic structure. Interestingly, the Mulliken spin population on iron does not decrease drastically upon reduction from $^5_2$1^6 (3.8) to $^3_0$1^5 (3.3). The electron density on the metal only slightly increases during the reduction process and the increase of electron density due to afm coupling is compensated by a ligand loss. The calculated reduction potential of −1.87 V is again in excellent agreement with experimental measurements.

The electronic structure of the four-coordinate complex $^3_0$1^4 is best described as a reduced bpy and a reduced pyridine ligand resulting in a doubly reduced chelate ligand framework which couples to a high-spin Fe(II) center as illustrated by the spin density in figure 6. A schematic diagram of the frontier MOs of $^3_0$1^4 is depicted in figure 4 (c). The species is 7.7 kcal/mol higher in energy than $^3_0$1^5, resulting in a calculated reduction potential of −2.20 V (deviation of −330 mV from experiment). However, both isomers exhibit significant spin contamination ($<S^2>(^3_0$1$^4) = 3.5$, $<S^2>$ $(^3_0$1$^4) = 3.2$ and $<S^2>$(triplet) = 2). Furthermore, the energy difference between the two isomers is strongly dependent on the choice of functional: ωB97M-V predicted the largest energy difference and PBE the smallest

at 1.8 kcal/mol.

All hybrid functionals tend to localize the additional electron density upon both reduction steps onto the ligand suggesting a doubly reduced ligand framework which couples to a high-spin Fe(II) center. In contrast, local functionals like PBE preferably delocalize more electron density at the metal center which would suggest a stronger afm (or metal based reduction). This is illustrated by the different spin densities obtained with ωB97M-V and PBE in figure 6. This finding is in agreement with current literature about the physical and formal oxidation states of the central metal in reduced complexes containing redox-active ligand frameworks like Fe(II) pyridine and bpy complexes.[103–106] Benchmark of density functionals against wave function methods showed in such cases a poor performance of hybrid functionals. The top performers were local functionals like PBE and TPSS which suggests that ωB97M-V is not an ideal choice for this doubly reduced intermediate.[104] Therefore, we employed CASSCF(8,7)/NEVPT2 to get insights into the static correlation in the electronic structure and an estimate of the energy difference between the two isomers (see SI for a detailed discussion). Both ${}^{3}_{0}1^{4}$ and ${}^{3}_{0}1^{5}$ revealed partial occupation numbers of the natural orbitals and confirm that these highly reduced Fe(II) pyridine complexes have some amount of static correlation.

The wave-function method predict a small gap of $\approx$2 kcal/mol and ${}^{3}_{0}1^{5}$ to be lower in energy (see SI for further details). An in-depth analysis of the electronic structure of these two possible intermediates using CASSCF is beyond the scope of this work.[107–111] However, this discussion should illustrate that ${}^{3}_{0}1^{4}$ and ${}^{3}_{0}1^{5}$ are likely closer in energy as predicted by the computational set up used in this study and thus are both accessible species. Overall, ${}^{3}_{0}1^{4}$ is most likely the key reactive intermediate in the catalytic cycle, and the active species for the binding and activation of CO_2 (*vide infra*). Both excess electrons are highly delocalized among the bpy π^* and py π^* and the metal center. The antiferromagnetic ordering in the electronic structure makes this intermediate challenging for KS-DFT. The ligand-based character of the reductions was reported with both experimental and computational evidence

by some of us for a similar polypyridine iron catalyst.[112]

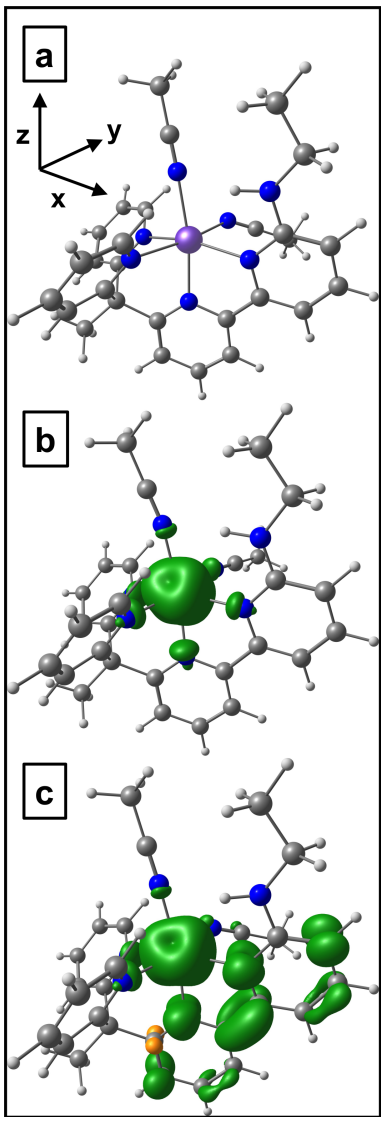

Figure 3: a) the optimized geometry of $[Fe(bpy^{NHEt}PY2\,Me)L_2]^{2+}$ ($^5_2 1^6$); b) spin density of $^5_2 1^6$ and c) spin densiity of the singly reduced intermediate $[Fe(bpy^{NHEt}PY2\,Me)L_2]^{+}$ ($^6_1 1^6$). In contrast to $^5_2 1^6$, the spin density on the ligand in $^6_1 1^6$ is non-zero, indicating that the first reduction is ligand-centered.

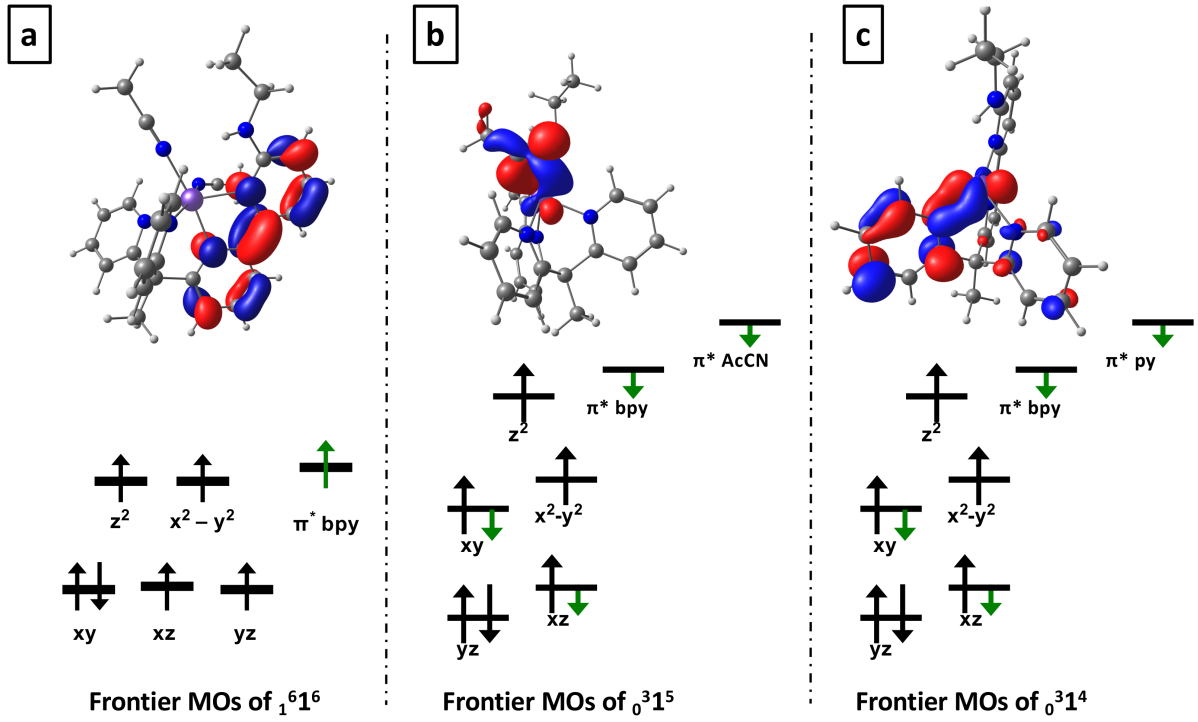

Figure 4: Schematic diagram of the frontier molecular orbitals of a) ${}^{6}_{1}1^{6}$ ($[\mathrm{Fe(bpy^{NHEt}PY2\,Me)L_2}]^{+}$), b) ${}^{3}_{0}1^{5}$ ($[\mathrm{Fe(bpy^{NHEt}PY2\,Me)}(\eta^2{-}\mathrm{NCCH_3})]^{0}$) and c) ${}^{3}_{0}1^{4}$ ($[\mathrm{Fe(bpy^{NHEt}PY2\,Me)}]^{0}$) including the key molecular orbitals for the reduction step. In (a) the α SOMO is a ligand centered, bpy π^*, consistent with fig. 3. The doubly reduced species shown in panels (b) and (c), exhibit antiferromangetic coupling between ligand and metal orbitals, leading to partial occupation and strong correlation (indicated by half-length arrows).

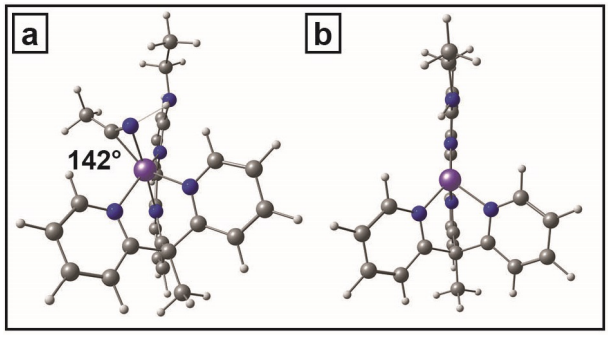

Figure 5: a) Geometry of five-coordinate doubly reduced complex ${}^{3}_{0}1^{5}$ ($[\mathrm{Fe(bpy^{NHEt}PY2\,Me)}(\eta^2{-}\mathrm{NCCH_3})]^{0}$) and b) the four-coordinate alternative ${}^{3}_{0}1^{4}$ ($[\mathrm{Fe(bpy^{NHEt}PY2\,Me)}]^{0}$).

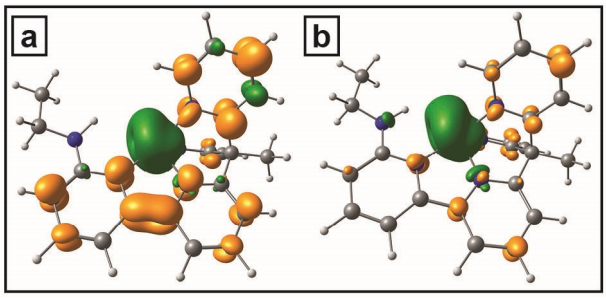

Figure 6: Spin density of ${}^{3}_{0}1^{4}$ ([Fe(bpy$^{\mathrm{NHEt}}$PY2Me)]^{0}) using the ωB97M-V (a) and the PBE (b) functionals, respectively. (α spin density green; β spin density yellow); ωB97M-V localizes most of the excess electron density in the ligand framework whereas PBE delocalizes the excess electrons strongly over both ligand and metal center resulting in significantly less spin density in the ligand moiety.

CO_2 Binding

There are four different binding modes for CO_2 to bind to a metal center: three restricted to an interaction between metal center and CO_2 and one involving a metal-ligand cooperation (MLC) (see figure 7). The following discussion focuses on the metal binding; metal ligand cooperation will be discussed in a later part of the manuscript.

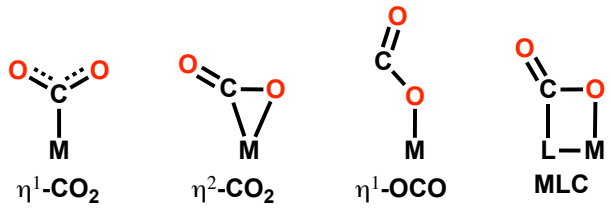

Figure 7: Schematic illustration of the four possible CO_2 binding modes (MLC = metal ligand cooperation).

The reaction pathway remains on the triplet surface and the lowest energy species $[Fe(bpy^{NHEt}PY2\,Me)(\eta^2{-}CO_2)]^0$ is a pentacoordinated CO_2 adduct in the η^2 binding mode ($^3_0 2^5$, see fig. 8 (a)) (the quintet species is 2.2 kcal/mol higher in energy). The OCO angle ($\angle$(OCO)) is 139°, which indicates at least partial reduction of the CO_2 fragment ($\angle$(OCO) is 134° for free $CO_2^{\cdot-}$). This is also confirmed by the spin density of $^3_0 2^5$ which shows significant excess spin in the CO_2 moiety (see figure S4). The $^3_0 2^5$ adduct is 2.4 kcal/mol lower in energy than the η^1-OCO isomer $[Fe(bpy^{NHEt}PY2\,Me)(CO_2{-}\kappa O)]^0$ ($^3_0 2^5(\eta^1\kappa O)$). This preference for the η^2 binding mode can be rationalized by analysing the electronic structure: the η^2 binding mode enables a σ interaction between the O lone pair and the Fe-d_{z^2} orbital (see the frontier MO in figure 8 (b)), a π interaction between the CO2 π^* orbital with a Fe-t_{2g} orbital (see the frontier MO in figure 8 (c)) and hydrogen bonding by the amine group. A dative bond σ bond is formed between the oxygen lone pair and a Fe-e_g type orbital (d_{z^2}). In total, three electrons occupy both bonding and anti bonding orbitals due to the high spin iron center. Thus, the interaction is still net stabilizing, the frontier anitbonding e_g^* (d_{z^2}) is depicted in figure 8 (b) (low lying bonding orbitals are depicted in figures S10 (a) and (b)). The occupied π^* orbital in the singly reduced CO_2 moiety can delocalize onto two Fe-t_{2g}

orbitals which are empty in the β space (figure 8 (c)). This interaction motif illustrates that the Fe center remains Lewis acidic, allowing an effective coordination of the oxygen.

Both reduced complexes ${}^{3}_{0}1^{5}$ and ${}^{3}_{0}1^{4}$ can act as the active species to bind and activate CO_2, the energetics and kinetics involving both species are summarized in table 2. In a first scenario, the binding of CO_2 to ${}^{3}_{0}1^{5}$ via an η^2 binding mode is slightly thermodynamically uphill and kinetically inhibited as the activation barrier is high. The geometry of the TS is illustrated in figure 9 (b) and involves not only the bond formation of both Fe$-CO_2$ and Fe$-$OCO bonds but also the simultaneous bond dissociation of the Fe$-$N and Fe$-$C bonds of the bound CH_3CN, rationalizing the high barrier. It is noteworthy that the amine group already forms a hydrogen bond to CO_2 at the TS. In a second scenario, CO_2 binds to ${}^{3}_{0}1^{4}$ via the η^2 binding mode which is thermodynamically favorable and the activation barrier is significantly lower because CO_2 can directly bind at the axial position with favorable hydrogen bonding (see figure 9 (a)). In a third scenario, CO_2 can bind via a η^1-OCO. However, this is not only thermodynamically less favorable but also kinetically inaccessible. In summary the analysis of the CO_2 adducts indicate that the active species for CO_2 binding is ${}^{3}_{0}1^{4}$ and the resulting adduct ${}^{3}_{0}2^{5}$ binds CO_2 in the η^2 binding mode including a stabilizing hydrogen bond from the amine group.

Table 2: Relative Gibbs free reaction energies and barriers for the formation of CO_2 adducts after the second reduction (energies in kcal/mol).
* using B97-D geometries because the TS could not be located with ωB97X-D.

Reaction			$\Delta_R G$	$\Delta G^{\ddagger}$
${}^{3}_{0}1^{5}$ + CO_2	$\longrightarrow$	${}^{3}_{0}2^{5}(\eta^2)$ + CH_3CN	2.1	25.4
${}^{3}_{0}1^{4}$ + CO_2	$\longrightarrow$	${}^{3}_{0}2^{5}(\eta^2)$	−5.7	9.5
${}^{3}_{0}1^{4}$ + CO_2	$\longrightarrow$	${}^{3}_{0}2^{5}(\eta^1\kappa O)$	−2.5	≈44*

Protonation of the CO_2 Adduct

The subsequent protonation of the reduced CO_2 significantly lowers the energy of the CO_2 π^* orbital, inducing a second charge transfer from the complex to COOH moiety. This

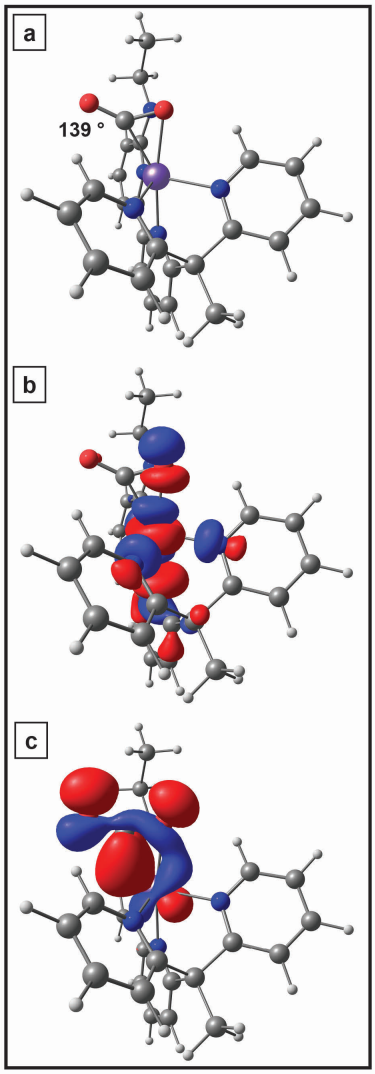

Figure 8: a) geometry of the CO_2 adduct ${}^{3}_{1}2^{5}$; b) MO illustrating the interaction of the oxygen lone pair with the metal d_{z2} orbital; c) MO illustrating the stabilization of the CO_2 π^* with a t_{2g} metal orbital via a π type interaction.

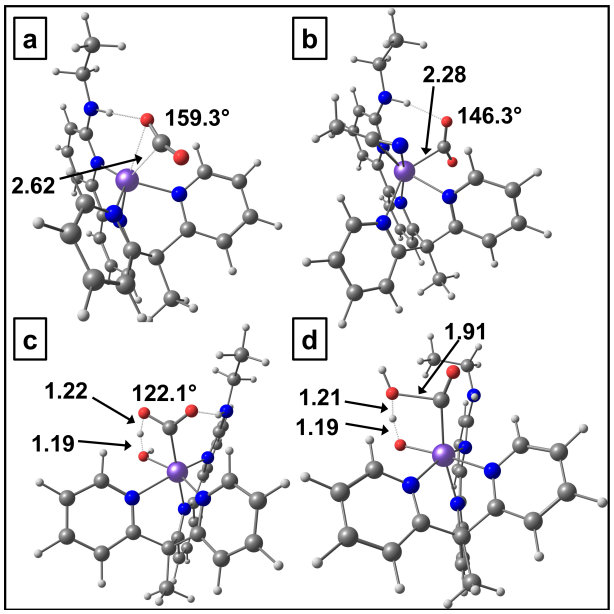

Figure 9: Geometries of the key transition states in the catalytic cycle: CO_2 addition to a) ${}^{3}_{0}1^{4}$, b) ${}^{3}_{0}1^{5}$, c) first protonation of ${}^{3}_{0}2^{5}$, d) second protonation of ${}^{5}_{1}3^{6}$, both protonation transition states utilize water as the proton source (distances in Å).

reduction of the CO_2 ligand is reflected in the smaller O-C-O bond angle of 118° (see SI fig S7). Upon protonation and charge transfer the bonding situation changes from a π type interaction of the $CO_2^{\cdot -}$ to a dative bond of the CO_2H^- lone pair as a σ-donor into the Fe-d_{z^2} orbital. This causes a change of the binding mode from η^2 to η^1-COO which leads to a small high-spin (S = 2) low-spin (S = 0) gap, similar to the unreduced catalyst species. The hexacoordinated carboxy species $[Fe(bpy^{NHEt}PY2\,Me)(CO_2H)L]^+$ in the low-spin configuration is the most stable intermediate (${}^{1}_{1}3^{6}$). However, the two high-spin isomers lie within 1.5 kcal/mol (${}^{5}_{1}3^{5}$: 0.5 kcal/mol and ${}^{5}_{1}3^{6}$: 1.5 kcal/mol). The advantage of the high-spin surfaces is the ability to undergo rapid ligand exchange associated with a geometry conversion from trigonal-bipyramidal to octahedral.

The open axial coordination site allows the CO_2 adduct ${}^{3}_{0}2^{5}$ to coordinate a water molecule as a sixth ligand, which opens up the possibility of a *intramolecular* proton transfer using H_2O. The formation of such a precomplex is only slightly endergonic (2.5 kcal/mol). The intramolecular protonation pathway leads to two major advantages: first, a perfect alignment of the H_2O and CO_2 molecules for the subsequent protonation due to a hydrogen- and a

dative bond of the water and the hydrogen bond of the amine group (see the TS geometry in figure 9 (c); second, the enhancement of the Brønsted acidity of the H_2O through binding to the Lewis acidic metal center. This polarizes the O–H bond and stabilizes the resulting base. Hence, the first protonation reaction yielding ${}^{5}_{1}3^{5}$ is facile both thermodynamically (−9.9 kcal/mol) and kinetically (barrierless). The first protonation step is also barrierless on the quintet surface (see table S3).

The second protonation is able to follow an intramolecular pathway as well. This is attributed to the fact that the energy difference between the five and six-coordinated carboxy intermediates is only 1.0 kcal/mol (*vide supra*). This facilitates the rapid ligand exchange featuring the removal of the leftover hydroxide ligand from the complex, followed by the coordination of a new water molecule. Alternatively, the hydroxide can also get protonated by another acid source in solution (e.g. H_2CO_3).

The second protonation step is accompanied by the cleavage of the C–O bond and results in H_2O and a metal carbonyl $[Fe(bpy^{NHEt}PY2\,Me)(CO)L]^{2+}$ (${}^{2}_{1}4^{6}$). The reaction is more likely to proceed on the quintet surface because it has a slightly lower barrier. However, both singlet and quintet surfaces have similar energetics and kinetics (see table 3). Similarly to the first protonation step, a coordinated water ligand benefits from an enhanced acidity due to the $Fe-OH_2$ bond and its optimized geometric alignment (see figure 9 (d)) yielding an exergonic process (−3.3 kcal). The intramolecular second proton transfer happens simultaneously with the heterolytic cleavage of the C–O bond and the release of one water molecule. The concerted bond formation and cleavage is crucial to compensate the kinetic penalty of the C–O bond splitting, which has been estimated to be 36 kcal/mol.[45] Thus, the intramolecular process has still a sizeable barrier with 8.9 kcal/mol. The barrier gets lowered by 2.7 kcal/mol if the proton source is H_2CO_3 which accelerates the this step by a factor of 100. In summary, an EEC mechanism is proposed with the CO_2 binding as the rate limiting step and the COOH intermediate as the resting state. The second protonation step is prohibited on the triple surface for both kinetic and thermodynamic reasons. The barrier for the second protonation

is 15.4 kcal/mol, 6.5 kcal/mol larger than the barrier along the quintet surface. Additionally, the triplet carboxy intermediate is 14 kcal/mol higher in energy than the quintet carboxy intermediate ${}^{5}_{1}3^{5}$, presumably because of an less preferred intermediate spin Fe center on the triplet surface.

The high oxidation state of iron (Fe(II)) in the resulting carbonyl intermediate ${}^{1}_{2}4^{6}$ rationalizes the exergonic nature of the CO release (−6.0 kcal/mol) to regenerate ${}^{5}_{2}1^{6}$ barrierless. The interaction is mainly driven by the σ forward-donation of the CO because the π back-donation is limited by the high oxidation state of the central metal. In addition, the CO release is further enhanced by the low solubility of CO in water which promotes its direct release into gas phase thus also reducing the likelihood of catalyst poisoning at this step in the cycle (*vide infra*). The free energy diagram of the complete catalytic pathway is depicted in figure 10.

Table 3: The activation energies and pK_a values of both protonation steps. The activation and reaction free energies correspond to the intramolecular proton transfer using H_2O (reactant) & OH^- (product) as a sixth ligand. The pK_a values refer to the equilibria using acetonitrile as a ligand and experimental free energy for H^+.

Reaction					$\Delta_R G$	$\Delta G^{\ddagger}$	pK_a
${}^{3}_{0}2^{5}$	$+H_2O$	$\longrightarrow$	${}^{5}_{0}3^{6OH}$		−9.9	-	26
${}^{5}_{1}3^{5}$	$+H_2O$	$\longrightarrow$	${}^{1}_{1}4^{6OH}$	$+ H_2O$	−3.3	8.9	15
${}^{5}_{1}3^{5}$	$+H_2CO_3$+L	$\longrightarrow$	${}^{1}_{2}4^{6}$	$+ H_2O$+HCO_3^-	−1.8	6.1	15
${}^{1}_{1}3^{6}$	$+H_2O$	$\longrightarrow$	${}^{1}_{1}4^{6OH}$	$+ H_2O$	−2.8	9.9	14

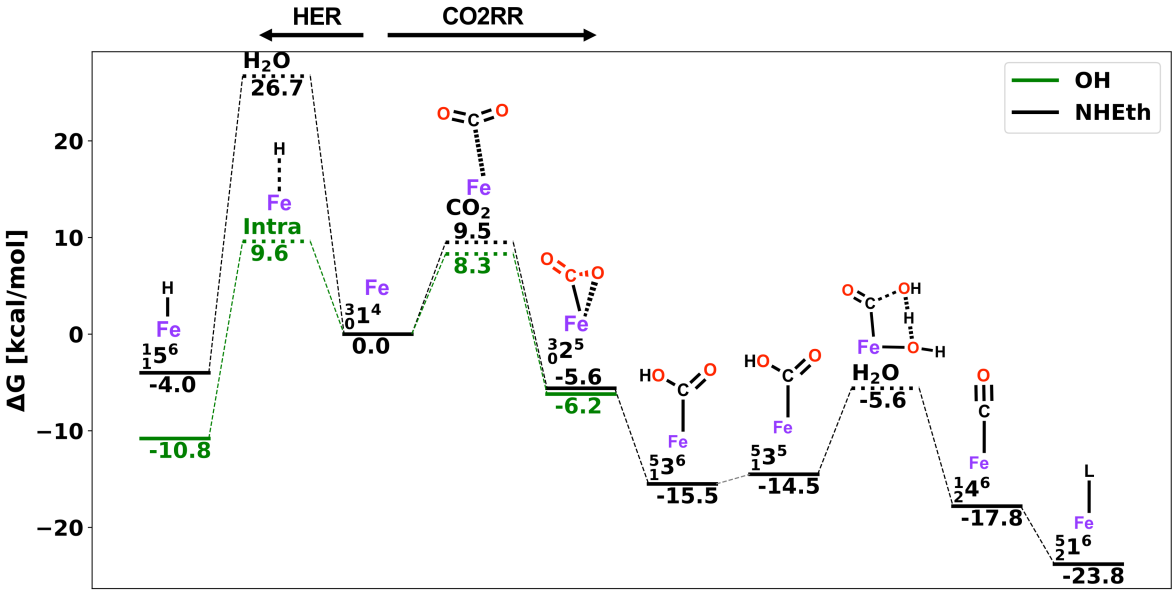

Figure 10: Free energy landscape of both CO2RR and HER pathways for $[Fe(bpy^{OH}PY2\,Me)L_2)]^{2+}$ (green) and $[Fe(bpy^{NHEt}PY2\,Me)L_2)]^{2+}$ (black); solid lines correspond to intermediate states and dashed line to a transition states; the sixth ligand L corresponds to CH_3CN, except for the two intramolecular protonation steps where water and hydroxide are used; assuming a rapid ligand exchange between both protonation steps (see main text for justification).

Possible Pathways Towards Catalyst Degradation and Activity Decrease

A high selectivity towards CO2RR versus HER is an important feature of a CO_2 reduction catalyst and is experimentally observed for the $[Fe(bpy^{NHEt}PY2\,Me)L_2]^{2+}$ system. It is a key feature of a good catalyst and can originate either from thermodynamics[45] or kinetics.[41,42] Furthermore, catalyst degradation tremendously reduces the efficiency of catalytic materials. Thus, both aspects should be understood and are investigated in this section.

A possible mechanism for HER involves the formation of a hydride $[HFe(bpy^{NHEt}PY2\,Me)L]$. The addition of a proton to ${}^{6}_{1}1^{6}$ results in the formation of a metal hydride intermediate (${}^{2}_{2}5^{6}$). Upon addition of the proton, a coincident oxidation of the metal center and $bpy^{\cdot -}$ takes place to form H^-. The hydride is a strong σ donor; hence, the resulting stronger d-orbital splitting stabilizes the low spin configuration. However, the formation of the complex ${}^{2}_{2}5^{6}$ is thermodynamically unfavorable and thus would require strong acidic conditions as the pK_a of the complex is negative. Thus, the formation of a hydride species can be ruled out after the first reduction step.

In contrast, the formation of a hydride species from ${}^{3}_{0}1^{4}$ is thermodynamically favorable with a pK_a of 33 which is higher than any pK_a in the CO2RR; using water as the proton source the free energy is -4.0 kcal/mol comparable to CO_2 addition. The resulting hydride species is hexacoordinated and low spin (${}^{1}_{1}5^{6}$). The two excess electrons localize to form a H^- and a Fe(II) metal center as the proton gets reduced by the two electrons delocalized over the metal and π^* orbital of the ligand framework. However, a high barrier (26.7 kcal/mol) for hydride formation with water as the proton source hinders HER kinetically. This barrier shrinks significantly (11.1 kcal/mol) using a moderately strong acid (H_2CO_3). Therefore, the main product of catalysis should be CO even when a moderately strong acid is added to the reaction mixture albeit with lower selectivity. The high selectivity even with moderately strong acids can be explained by the electronic structure of ${}^{3}_{0}1^{4}$. The highly delocalized excess electrons and the low coordination number results in a Lewis acidic and positively

charged metal center. On the one hand, CO_2 has a high quadruple moment allowing for a facile coordination via the oxygen resulting in a lower barrier (9.5 kcal/mol). On the other hand, the coordination of an acid (via hydrogen) to a Lewis acid metal center results in a high barrier. Thus, despite being thermodynamically favored, the addition of H^+ even with an acidic proton source (H_2CO_3) is about 15 times slower than CO_2.

A third reduction is a possible degradation pathway because the dissociation of CO from a singly reduced carbonyl intermediate is significantly endergonic ($\Delta_R G = 9.6$ kcal/mol, but barrierless) and could consequently trap the catalyst, especially in solvents with higher CO solubility than acetonitrile. This CO poisoning was observed and proposed for the nickel cyclam system.[45,47] A third reduction can happen at various stages of the catalytic cycle: First, the reduction of the CO_2 adduct is unlikely as the reduction potential is -2.16 V vs Fc/Fc^+ which is more negative than the two reductions of ${}^{5}_{2}1^{6}$. In addition, the protonation processes utilize H_2O as an intramolecular proton source; therefore, the lifetime of these species is expected to be short and make an additional reduction less likely. Second, the reduction of the carboxy intermediate ${}^{5}_{1}3^{5}$ yielding ${}^{4}_{0}3^{5}$ (-1.81 V) is feasible because the potential is less negative than the potential required to obtain ${}^{3}_{0}1^{5}$. Third, the carbonyl intermediate ${}^{1}_{2}4^{6}$ can readily be reduced to ${}^{4}_{1}4^{5}$ (-1.00 V) because the excess electron increases the backbonding of CO as indicated by the red-shift of 136 cm^{-1} in the carbonyl stretching mode.

The bent acetonitrile in ${}^{3}_{0}1^{5}$ suggests a protonation of the activated acetonitrile may be possible (see figures S1 (a) & (b)). However, the protonation is kinetically inhibited using H_2O as the proton source with a barrier over 30 kcal/mol. The transition state for the possible intramolecuar protonation of the activated CH_3CN is depicted in figure S9. Therefore, ${}^{3}_{0}1^{5}$ is kinetically inhibited for the reaction with both CO_2 and H_2O.

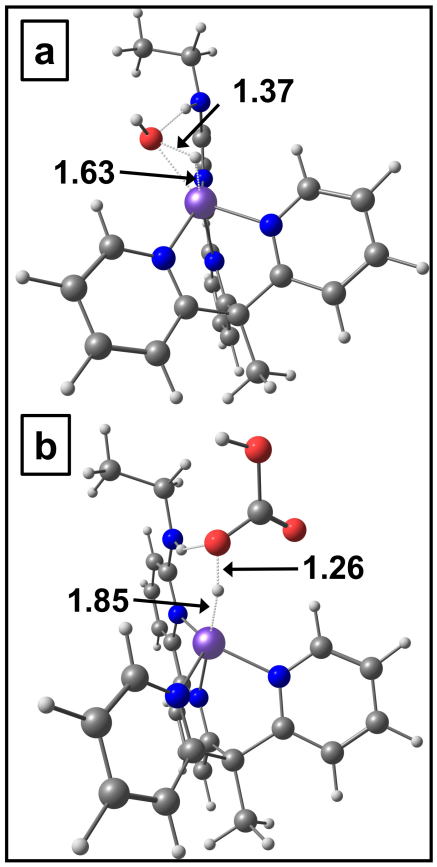

Figure 11: Geometries of for the transition states for a possible formation of a hydride using (a) water and (b) carbonic acid as the proton source (distances in Ångstrom).

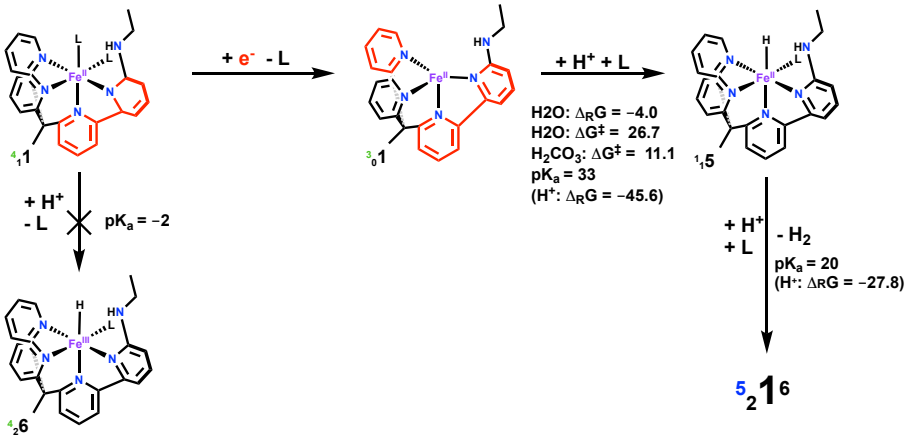

Figure 12: Possible HER mechanism involving $[Fe(bpy^{NHEt}PY2\,Me)L_2)]^{2+}$ starting from the doubly reduced ${}^{3}_{0}1^{4}$. The red colored molecular moiety indicate localization of the excess electrons; reaction and activation energies in kcal/mol; reduction potentials against Fc/Fc^{+}; L = CH_3CN.

Hydroxyl Substituent

The hydroxyl substituent complex $[Fe(bpy^{OH}PY2\,Me)L_2)]^{2+}$ showed a high Faradaic efficiency but low selectivity. In bulk electrolysis, significant amounts of both CO and H_2 were observed. The lower selectivity of the can be related to the increased acidity of the second coordination sphere. The doubly reduced active species of $[Fe(bpy^{OH}PY2\,Me)L_2)]^{2+}$ (${}^{3}_{0}1^{4OH}$) has two competing pathways with similar activation barriers: an *intramolecuar* proton transfer and CO_2 addition.

On the one hand, the high acidity of the hydroxyl group opens up the possibility of an intramolecular proton transfer for ${}^{3}_{0}1^{4OH}$ from the hydroxyl group to the Fe center with an activation energy of 9.6 kcal/mol. The transition state is shown in figure 13 (a). This process yields a hydride which is an important intermediate for HER. On the other hand, the addiction of CO_2 to ${}^{3}_{0}1^{4OH}$ has a slightly lower barrier of 8.3 kcal/mol and results in the CO2RR pathway. The transition state is depicted in figure 13 (b). Thus, the stronger hydrogen bonding further facilitates CO_2 binding as the barrier is lower than for the NHEt isomers (9.5 kcal/mol) but dramatically decreases selectivity by opening up a facile HER pathway. This situation is illustrated in a free energy diagram of the two reaction pathways

in figure 10 for both the OH and NHEt substituent.

Alternative Catalysis Cycles

In addition to the discussed catalysis cycle, two alternative pathways are conceivable which either originate due to the binding of CO_2 to an alternative species formed during the catalysis cycle or stem from an altered CO_2 binding mode. They will be described in the following section, which includes a discussion about their limitations with respect to the proposed catalytic cycle.

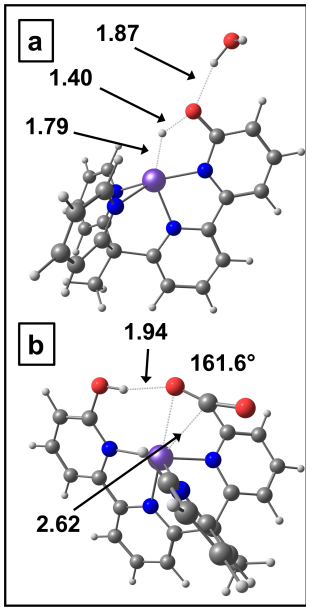

Figure 13: Geometries of the and key parameters of the transition states for a) intramolecular proton transfer and b) CO_2 addition of $[Fe(bpy^{OH}PY2)\,L_2Me)]^{2+}$ (distances in Å).

1. CO_2 could also bind to the singly reduced species ${}^{6}_{1}1^{6}$ by replacing a solvent ligand suggesting an ECE mechanism. The most stable isomer is a six-coordinated quartet state with CO_2 in an η^2 mode (${}^{4}_{1}2^{6}$). The CO_2 activation process is endergonic (4.6 kcal/mol) implying that the species could exist in equilibrium. The reaction barrier of this step is 13.8 kcal/mol making it the rate limiting step in this cycle. The calculated potential for the reduction of the CO_2 adduct ${}^{4}_{1}2^{6}$ to ${}^{3}_{0}2^{5}$ is -1.76 V vs Fc/Fc^{+} which is in very good agreement

with the experimentally applied potential. The subsequent protonation of ${}^{3}_{0}2^{5}$ is identical to the proposed catalytic cycle. It is noteworthy that no singly reduced CO_2 adducts could be computed for the parent compound revealing that in this case the amine group is crucial for the CO_2 binding. In summary, it is both thermodynamically and kinetically less favorable to bind CO_2 after only 1 initial reduction. The rate limiting step remains the CO_2 addition and the resting states remains the carboxy adduct.

2. Alternatively to the formation of a solely metal-bound adduct, CO_2 can also cooperatively bind to the ligand framework (see figure 7). This was observed in several other cases e.g. pincer-type complexes[113–115] zirconium metallocene phosphinoaryloxide complex[116] as well as in catalytic processes.[117,118] There are two conceivable ligand-based binding sites for CO_2 in this ligand framework; it can be inserted into the amine group yielding a carbamate or can bind via a reversible C–C bond to the ligand framework (see fig. 14).

In a first scenario, CO_2 is bound to the amine group. However, the formation of this carbamate intermediate is not favorable in comparison to a metal bound CO_2 adduct (8.6 kcal/mol). In addition, it readily rearranges to a metal-hydride via an intramolecular proton transfer ($\Delta G_R = -22.8$ kcal/mol). The nucleophilic character of the hydride would either favor the hydrogen evolution upon addition of a second proton or the formation of formic acid over the experimentally observed CO.

In a second scenario, CO_2 can bind via a *reversible* C–C bond to a pyridine forming an sp^3-C2 carbon in the ring (${}^{5}_{0}2^{5CC}$ see fig. S7). This intermediate is the most stable isomer in the CO_2 adduct isomer-space as it is more than 20 kcal/mol lower in energy than the metal bound adducts in all spin states. A mechanism using this species is conceivable via an aromatization/dearomatization sequence as the second reduction to ${}^{3}_{0}1^{4}$ already breaks the aromaticity in the pyridine (*vide supra*). Both protonation steps are possible (pK_a = 12, 15) and the second protonation leads to a concerted O–H bond formation and C-C and C-O bond cleavage yielding H_2O, CO and the starting complex ${}^{5}_{2}1^{6}$. The regaining of aromaticity seems to be the main driving force for the C-C bond cleavage. However, ${}^{5}_{0}2^{5CC}$

is only accessible from ${}^{3}_{0}2^{5}(\eta^1\kappa\mathrm{O})$ ($[\mathrm{Fe(bpy^{NHEt}PY2\,Me)(CO_2{-}\kappa O)}]^0$) (see figure S5) which is an unlikely intermediate. The discussion about CO_2 adducts (*vide supra*) ruled out a direct formation of the η^1-OCO adduct. But it was not possible to locate a transition state connecting to the η^2 adduct (${}^{3}_{0}1^{5}$) or binding CO_2 directly in the metal ligand cooperation (MLC) binding mode. However, the energy difference between both CO_2 adducts (${}^{3}_{0}1^{5}(\eta^2)$ and ${}^{3}_{0}2^{5}(\eta^1\kappa\mathrm{O})$) is 2.4 kcal/mol. Therefore, if the lifetime of ${}^{3}_{0}2^{5}$ would be sufficiently long, an equilibrium could form between both binding modes. This would open up the possibility to enter the CC pathway. However, the proposed cycle predicts a very facile and fast first protonation step which makes the formation of the ${}^{5}_{0}2^{5\mathrm{CC}}$ intermediate unlikely.

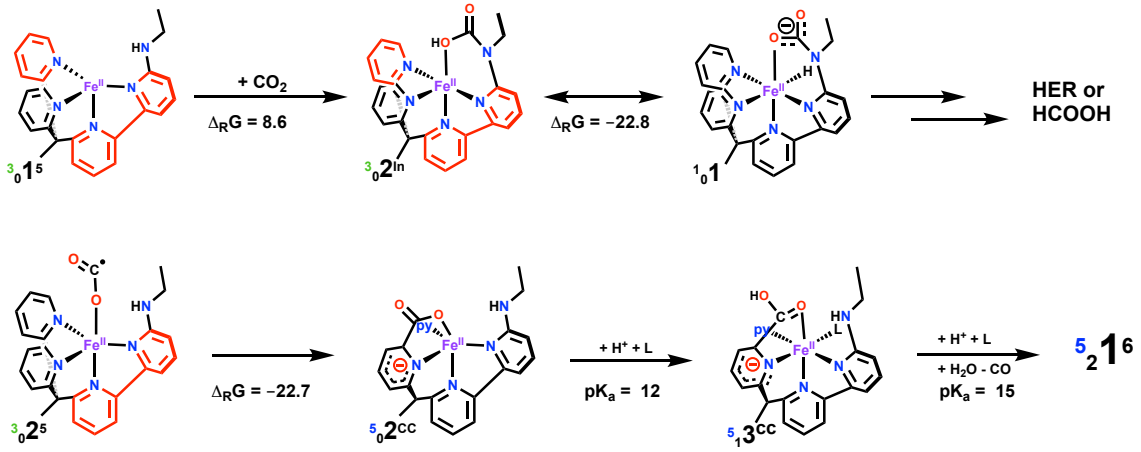

Figure 14: Alternative cycles involving cooperatively bound CO_2.

Conclusion

Electronic structure calculations were performed in order to study the electrochemical reduction of CO_2 to CO by $[Fe(bpy^{NHEt}PY2\,Me)L_2]^{2+}$. A schematic free energy diagram summarizing the results is depicted in figure 10. The redox active ligand framework paired with a high spin Fe(II) center allows effective delocalization of additional electrons rationalizing the reduction events at mild negative potentials. The metal center remains Lewis acidic through the reduction process because of the non-innocent chelate ligand framework and the ability to dissociate up to two solvent ligands. The high Lewis acidity of the Fe in the doubly reduced intermediate results in a high barrier for the formation of a hydride intermediate. In contrast, the binding of CO_2 is facile due to its high quadruple moment uncovering the origin of the selectivity in the kinetics. The CO_2 adduct exhibits an η^2 binding mode to maximize the π-type coupling of the singly reduced CO_2 π^* to a t_{2g}-type d-orbital. The Lewis acidity of the central metal allows further charge delocalization via a dative bond of the oxygen to the metal center. Furthermore, the amine group forms a favorable hydrogen bond to stabilize the CO_2 adduct.

The second available equatorial coordination site opens up the possibility of *intramolecular* protonation by coordination of H_2O. The formation of this precomplex facilitates protonation because not only CO_2 but also the proton source H_2O is activated due to the $Fe-OH_2$ bond. This polarizes the O–H bond and aligns both CO_2 and H_2O properly, resulting in a barrier-less first protonation. The small ligand field results in a high spin quintet surface for both protonation steps. The energy difference between the five and hexacoordinated carboxy intermediates is small which allows a rapid ligand exchange for a second intramolecular protonation. This step exhibits a concerted heterolytic cleavage of the C-O bond and the release of a water molecule. The resulting carbonyl species is only weakly bound due to the high oxidation state and weak ligand field; thus, the CO release is exergonic to recover the initial state of the catalyst. The proposed mechanism follows an EEC mechanism with the formation of the CO_2 adduct as the rate-limiting step. This rationalized the importance of

the second coordination sphere.

The lower selectivity of the corresponding hydroxy-substituted complex $[Fe(bpy^{OH}PY2\,Me)L_2]^{2+}$ is connected to the higher acidity of the hydroxyl group as it opens up the possibility of an intramolcular proton transfer to form a hydride intermediate. This barrier is even lower than protonation with an acid source (H_2CO_3) and has a similar magnitude than CO_2 addition. This rationalizes the experimental finding that $[Fe(bpy^{OH}PY2\,Me)L_2]^{2+}$ produces both CO and H_2.

Acknowledgement

Part of this material is based upon work performed by the Joint Center for Artificial Photosynthesis, a DOE Energy Innovation Hub, supported through the Office of Science of the U.S. Department of Energy under Award Number DE-SC0004993. This work was also supported by the U.S. Department of Energy, Office of Science, Office of Advanced Scientific Computing, and Office of Basic Energy Sciences, via the Scientific Discovery through Advanced Computing (SciDAC) program. C.J.C. was supported by DOE/LBNL Grant 101528-002 and is CIFAR Fellow. We thank Ainara Nova, Joonho Lee and Jeff Derrick for fruitful discussions.

References

(1) Global Energy Statistical Yearbook, Total energy consumption. 2019.

(2) Concepcion, J. J.; House, R. L.; Papanikolas, J. M.; Meyer, T. J. Chemical approaches to artificial photosynthesis. *Proc. Natl. Acad. Sci.* **2012**, *109*, 15560–15564, DOI: 10.1073/pnas.1212254109.

(3) Alstrum-Acevedo, J. H.; Brennaman, M. K.; Meyer, T. J. Chemical Ap-

proaches to Artificial Photosynthesis. 2. *Inorg. Chem.* **2005**, *44*, 6802–6827, DOI: 10.1021/ic050904r.

(4) Appel, A. M. et al. Frontiers, Opportunities, and Challenges in Biochemical and Chemical Catalysis of CO2 Fixation. *Chem. Rev.* **2013**, *113*, 6621–6658, DOI: 10.1021/cr300463y.

(5) Schuchmann, K.; Müller, V. Direct and Reversible Hydrogenation of CO2 to Formate by a Bacterial Carbon Dioxide Reductase. *Science* **2013**, *342*, 1382–1385.

(6) Wang, W.; Wang, S.; Ma, X.; Gong, J. Recent advances in catalytic hydrogenation of carbon dioxide. *Chem. Soc. Rev.* **2011**, *40*, 3703–3727.

(7) Habisreutinger, S. N.; Schmidt-Mende, L.; Stolarczyk, J. K. Photocatalytic Reduction of CO2 on TiO2 and Other Semiconductors. *Angew. Chem., Int. Ed.* **2013**, *52*, 7372–7408.

(8) Grice, K. A.; Kubiak, C. P. *CO2 Chemistry*; Advances in Inorg. Chem.; Academic Press, 2014; Vol. 66; pp 163–188.

(9) Qiao, J.; Liu, Y.; Hong, F.; Zhang, J. A review of catalysts for the electroreduction of carbon dioxide to produce low-carbon fuels. *Chem. Soc. Rev.* **2014**, *43*, 631–675.

(10) Zhao, G.; Huang, X.; Wang, X.; Wang, X. Progress in catalyst exploration for heterogeneous CO2 reduction and utilization: a critical review. *J. Mater. Chem. A* **2017**, *5*, 21625–21649, DOI: 10.1039/C7TA07290B.

(11) Verma, S.; Kim, B.; Jhong, H.-R. â.; Ma, S.; Kenis, P. J. A. A Gross-Margin Model for Defining Technoeconomic Benchmarks in the Electroreduction of CO2. *ChemSusChem* **2016**, *9*, 1972–1979.

(12) de Klerk, A.; Furimsky, E. Catalysis in the refining of Fischer–Tropsch syncrude. *Platinum Metals Rev* **2011**, *55*, 263–267.

(13) Kuhl, K. P.; Cave, E. R.; Abram, D. N.; Jaramillo, T. F. New insights into the electrochemical reduction of carbon dioxide on metallic copper surfaces. *Energy Environ. Sci.* **2012**, *5*, 7050–7059, DOI: 10.1039/C2EE21234J.

(14) Lee, C. H.; Kanan, M. W. Controlling H+ vs CO2 Reduction Selectivity on Pb Electrodes. *ACS Catal.* **2015**, *5*, 465–469, DOI: 10.1021/cs5017672.

(15) Goodpaster, J. D.; Bell, A. T.; Head-Gordon, M. Identification of Possible Pathways for C-C Bond Formation during Electrochemical Reduction of CO2: New Theoretical Insights from an Improved Electrochemical Model. *J. Phys. Chem. Lett* **2016**, *7*, 1471–1477, DOI: 10.1021/acs.jpclett.6b00358.

(16) Medina-Ramos, J.; Pupillo, R. C.; Keane, T. P.; DiMeglio, J. L.; Rosenthal, J. Efficient Conversion of CO2 to CO Using Tin and Other Inexpensive and Easily Prepared Post-Transition Metal Catalysts. *J. Am. Chem. Soc.* **2015**, *137*, 5021–5027, DOI: 10.1021/ja5121088.

(17) Garza, A. J.; Bell, A. T.; Head-Gordon, M. Mechanism of CO2 reduction at copper surfaces: Pathways to C2 products. *ACS Catal.* **2018**, *8*, 1490–1499.

(18) Smieja, J. M.; Sampson, M. D.; Grice, K. A.; Benson, E. E.; Froehlich, J. D.; Kubiak, C. P. Manganese as a Substitute for Rhenium in CO2 Reduction Catalysts: The Importance of Acids. *Inorg. Chem.* **2013**, *52*, 2484–2491.

(19) Chen, L.; Guo, Z.; Wei, X.-G.; Gallenkamp, C.; Bonin, J.; Anxolabéhère-Mallart, E.; Lau, K.-C.; Lau, T.-C.; Robert, M. Molecular Catalysis of the Electrochemical and Photochemical Reduction of CO2 with Earth-Abundant Metal Complexes. Selective Production of CO vs HCOOH by Switching of the Metal Center. *J. Am. Chem. Soc.* **2015**, *137*, 10918–10921, DOI: 10.1021/jacs.5b06535.

(20) Roy, S.; Sharma, B.; Pécaut, J.; Simon, P.; Fontecave, M.; Tran, P. D.; Derat, E.; Artero, V. Molecular Cobalt Complexes with Pendant Amines for Selective Electro-

catalytic Reduction of Carbon Dioxide to Formic Acid. *J. Am. Chem. Soc.* **2017**, *139*, 3685–3696, DOI: 10.1021/jacs.6b11474.

(21) Wang, M.; Torbensen, K.; Salvatore, D.; Ren, S.; Joulié, D.; Dumoulin, F.; Mendoza, D.; Lassalle-Kaiser, B.; Işci, U.; Berlinguette, M. R., Curtis P. Berlinguette CO 2 electrochemical catalytic reduction with a highly active cobalt phthalocyanine. *Nat. Commun* **2019**, *10*, 1–8.

(22) Costentin, C.; Drouet, S.; Robert, M.; Savéant, J.-M. A Local Proton Source Enhances CO2 Electroreduction to CO by a Molecular Fe Catalyst. *Science* **2012**, *338*, 90–94, DOI: 10.1126/science.1224581.

(23) Beley, M.; Collin, J. P.; Ruppert, R.; Sauvage, J. P. Electrocatalytic reduction of carbon dioxide by nickel cyclam2+ in water: study of the factors affecting the efficiency and the selectivity of the process. *J. Am. Chem. Soc.* **1986**, *108*, 7461–7467, DOI: 10.1021/ja00284a003.

(24) Takeda, H.; Cometto, C.; Ishitani, O.; Robert, M. Electrons, Photons, Protons and Earth-Abundant Metal Complexes for Molecular Catalysis of CO2 Reduction. *ACS Catal.* **2017**, *7*, 70–88.

(25) Wu, Y.; Jiang, J.; Weng, Z.; Wang, M.; Broere, D. L. J.; Zhong, Y.; Brudvig, G. W.; Feng, Z.; Wang, H. Electroreduction of CO2 Catalyzed by a Heterogenized Zn-Porphyrin Complex with a Redox-Innocent Metal Center. *ACS Cent. Sci.* **2017**, *3*, 847–852.

(26) Lin, S.; Diercks, C. S.; Zhang, Y.-B.; Kornienko, N.; Nichols, E. M.; Zhao, Y.; Paris, A. R.; Kim, D.; Yang, P.; Yaghi, O. M.; Chang, C. J. Covalent organic frameworks comprising cobalt porphyrins for catalytic CO2 reduction in water. *Science* **2015**, *349*, 1208–1213, DOI: 10.1126/science.aac8343.

(27) Hod, I.; Sampson, M. D.; Deria, P.; Kubiak, C. P.; Farha, O. K.; Hupp, J. T. Fe-Porphyrin-Based Metal-Organic Framework Films as High-Surface Concentration, Heterogeneous Catalysts for Electrochemical Reduction of CO2. *ACS Catal.* **2015**, *5*, 6302–6309, DOI: 10.1021/acscatal.5b01767.

(28) Kornienko, N.; Zhao, Y.; Kley, C. S.; Zhu, C.; Kim, D.; Lin, S.; Chang, C. J.; Yaghi, O. M.; Yang, P. Metal-Organic Frameworks for Electrocatalytic Reduction of Carbon Dioxide. *J. Am. Chem. Soc.* **2015**, *137*, 14129–14135, DOI: 10.1021/jacs.5b08212.

(29) Elgrishi, N.; Griveau, S.; Chambers, M. B.; Bedioui, F.; Fontecave, M. Versatile functionalization of carbon electrodes with a polypyridine ligand: metallation and electrocatalytic H^+ and CO2 reduction. *Chem. Commun.* **2015**, *51*, 2995–2998, DOI: 10.1039/C4CC10027A.

(30) Oh, S.; Gallagher, J. R.; Miller, J. T.; Surendranath, Y. Graphite-Conjugated Rhenium Catalysts for Carbon Dioxide Reduction. *J. Am. Chem. Soc.* **2016**, *138*, 1820–1823, DOI: 10.1021/jacs.5b13080.

(31) Ren, S.; Joulié, D.; Salvatore, D.; Torbensen, K.; Wang, M.; Robert, M.; Berlinguette, C. P. Molecular electrocatalysts can mediate fast, selective CO2 reduction in a flow cell. *Science* **2019**, *365*, 367–369.

(32) Kumar, B.; Llorente, M.; Froehlich, J.; Dang, T.; Sathrum, A.; Kubiak, C. P. Photochemical and photoelectrochemical reduction of CO2. *Annual review of physical chemistry* **2012**, *63*, 541–569.

(33) Smieja, J. M.; Kubiak, C. P. Re(bipy-tBu)(CO)3Cl–improved Catalytic Activity for Reduction of Carbon Dioxide: IR-Spectroelectrochemical and Mechanistic Studies. *Inorg. Chem.* **2010**, *49*, 9283–9289.

(34) Smieja, J. M.; Benson, E. E.; Kumar, B.; Grice, K. A.; Seu, C. S.; Miller, A. J. M.; Mayer, J. M.; Kubiak, C. P. Kinetic and structural studies, origins of selectivity, and interfacial charge transfer in the artificial photosynthesis of CO. *Proc. Natl. Acad. Sci.* **2012**, *109*, 15646–15650.

(35) Benson, E. E.; Sampson, M. D.; Grice, K. A.; Smieja, J. M.; Froehlich, J. D.; Friebel, D.; Keith, J. A.; Carter, E. A.; Nilsson, A.; Kubiak, C. P. The Electronic States of Rhenium Bipyridyl Electrocatalysts for CO2 Reduction as Revealed by X-ray Absorption Spectroscopy and Computational Quantum Chemistry. *Angew. Chem., Int. Ed.* **2013**, *52*, 4841–4844.

(36) Sampson, M. D.; Froehlich, J. D.; Smieja, J. M.; Benson, E. E.; Sharp, I. D.; Kubiak, C. P. Direct observation of the reduction of carbon dioxide by rhenium bipyridine catalysts. *Energy. Environ. Sci.* **2013**,

(37) Sampson, M. D.; Nguyen, A. D.; Grice, K. A.; Moore, C. E.; Rheingold, A. L.; Kubiak, C. P. Manganese Catalysts with Bulky Bipyridine Ligands for the Electrocatalytic Reduction of Carbon Dioxide: Eliminating Dimerization and Altering Catalysis. *J. Am. Chem. Soc.* **2014**, *136*, 5460–5471, DOI: 10.1021/ja501252f.

(38) Machan, C. W.; Sampson, M. D.; Chabolla, S. A.; Dang, T.; Kubiak, C. P. Developing a Mechanistic Understanding of Molecular Electrocatalysts for CO2 Reduction using Infrared Spectroelectrochemistry. *Organometallics* **2014**, *33*, 4550–4559, DOI: 10.1021/om500044a.

(39) Machan, C. W.; Stanton, C. J.; Vandezande, J. E.; Majetich, G. F.; Schaefer, H. F.; Kubiak, C. P.; Agarwal, J. Electrocatalytic Reduction of Carbon Dioxide by Mn(CN)(2,2'-bipyridine)(CO)3: CN Coordination Alters Mechanism. *Inorg. Chem.* **2015**, *54*, 8849–8856, DOI: 10.1021/acs.inorgchem.5b01715.

(40) Sung, S.; Li, X.; Wolf, L. M.; Meeder, J. R.; Bhuvanesh, N. S.; Grice, K. A.;

Panetier, J. A.; Nippe, M. Synergistic Effects of Imidazolium-Functionalization on fac-Mn (CO) 3 Bipyridine Catalyst Platforms for Electrocatalytic Carbon Dioxide Reduction. *J. Am. Chem. Soc.* **2019**, *141*, 6569–6582.

(41) Keith, J. A.; Grice, K. A.; Kubiak, C. P.; Carter, E. A. Elucidation of the Selectivity of Proton-Dependent Electrocatalytic CO2 Reduction by fac-Re(bpy)(CO)3Cl. *J. Am. Chem. Soc.* **2013**, *135*, 15823–15829.

(42) Riplinger, C.; Sampson, M. D.; Ritzmann, A. M.; Kubiak, C. P.; Carter, E. A. Mechanistic Contrasts between Manganese and Rhenium Bipyridine Electrocatalysts for the Reduction of Carbon Dioxide. *J. Am. Chem. Soc.* **2014**, *136*, 16285–16298.

(43) Riplinger, C.; Carter, E. A. Influence of weak Brønsted acids on electrocatalytic CO2 reduction by manganese and rhenium bipyridine catalysts. *ACS Catal.* **2015**, *5*, 900–908.

(44) Beley, M.; Collin, J. P.; Ruppert, R.; Sauvage, J. P. Electrocatalytic reduction of carbon dioxide by nickel cyclam2+ in water: study of the factors affecting the efficiency and the selectivity of the process. *J. Am. Chem. Soc.* **1986**, *108*, 7461–7467, DOI: 10.1021/ja00284a003.

(45) Song, J.; Klein, E. L.; Neese, F.; Ye, S. The Mechanism of Homogeneous CO2 Reduction by Ni(cyclam): Product Selectivity, Concerted Proton-Electron Transfer and C-O Bond Cleavage. *Inorg. Chem.* **2014**, *53*, 7500–7507.

(46) Kelly, C. A.; Mulazzani, Q. G.; Blinn, E. L.; Rodgers, M. A. J. Kinetics of CO Addition to Ni(cyclam)+ in Aqueous Solution. *Inorg. Chem.* **1996**, *35*, 5122–5126, DOI: 10.1021/ic951527t.

(47) Froehlich, J. D.; Kubiak, C. P. The Homogeneous Reduction of CO2 by [Ni(cyclam)]+: Increased Catalytic Rates with the Addition of a CO Scavenger. *J. Am. Chem. Soc.* **2015**, *137*, 3565–3573.

(48) Costentin, C.; Passard, G.; Robert, M.; Savéant, J.-M. Ultraefficient homogeneous catalyst for the CO2-to-CO electrochemical conversion. *Proc. Natl. Acad. Sci.* **2014**, *111*, 14990–14994, DOI: 10.1073/pnas.1416697111.

(49) Römelt, C.; Song, J.; Tarrago, M.; Rees, J. A.; van Gastel, M.; Weyhermüller, T.; DeBeer, S.; Bill, E.; Neese, F.; Ye, S. Electronic Structure of a Formal Iron(0) Porphyrin Complex Relevant to CO2 Reduction. *Inorg. Chem.* **2017**, *56*, 4745–4750, DOI: 10.1021/acs.inorgchem.7b00401.

(50) Bonin, J.; Maurin, A.; Robert, M. Molecular catalysis of the electrochemical and photochemical reduction of CO2 with Fe and Co metal based complexes. Recent advances. *Coord. Chem. Rev.* **2017**, *334*, 184–198.

(51) Fukuzumi, S.; Lee, Y.-M.; Ahn, H. S.; Nam, W. Mechanisms of catalytic reduction of CO 2 with heme and nonheme metal complexes. *Chemical science* **2018**, *9*, 6017–6034.

(52) Davethu, P. A.; de Visser, S. P. CO2 Reduction on an Iron-Porphyrin Center: A Computational Study. *The Journal of Physical Chemistry A* **2019**, *123*, 6527–6535.

(53) Costentin, C.; Passard, G.; Robert, M.; Savéant, J.-M. Pendant Acid-Base Groups in Molecular Catalysts: H-Bond Promoters or Proton Relays? Mechanisms of the Conversion of CO2 to CO by Electrogenerated Iron(0)Porphyrins Bearing Prepositioned Phenol Functionalities. *J. Am. Chem. Soc.* **2014**, *136*, 11821–11829, DOI: 10.1021/ja506193v.

(54) Costentin, C.; Drouet, S.; Passard, G.; Robert, M.; Savéant, J.-M. Proton-Coupled Electron Transfer Cleavage of Heavy-Atom Bonds in Electrocatalytic Processes. Cleavage of a C-O Bond in the Catalyzed Electrochemical Reduction of CO2. *J. Am. Chem. Soc.* **2013**, *135*, 9023–9031, DOI: 10.1021/ja4030148.

(55) Nichols, A. W.; Machan, C. W. Secondary-Sphere Effects in Molecular Electrocatalytic CO2 Reduction. *FRONT CHEM* **2019**, *7*.

(56) Haviv, E.; Azaiza-Dabbah, D.; Carmieli, R.; Avram, L.; Martin, J. M.; Neumann, R. A thiourea tether in the second coordination sphere as a binding site for CO2 and a proton donor promotes the electrochemical reduction of CO2 to CO catalyzed by a rhenium bipyridine-type complex. *J. Am. Chem. Soc.* **2018**, *140*, 12451–12456.

(57) Hong, D.; Tsukakoshi, Y.; Kotani, H.; Ishizuka, T.; Kojima, T. Visible-Light-Driven Photocatalytic CO2 Reduction by a Ni(II) Complex Bearing a Bioinspired Tetradentate Ligand for Selective CO Production. *J. Am. Chem. Soc.* **2017**, *139*, 6538–6541.

(58) Dubey, A.; Nencini, L.; Fayzullin, R. R.; Nervi, C.; Khusnutdinova, J. R. Bio-Inspired Mn(I) Complexes for the Hydrogenation of CO2 to Formate and Formamide. *ACS Catal.* **2017**, *7*, 3864–3868.

(59) Dutta, A.; Lense, S.; Hou, J.; Engelhard, M. H.; Roberts, J. A. S.; Shaw, W. J. Minimal Proton Channel Enables H2 Oxidation and Production with a Water-Soluble Nickel-Based Catalyst. *J. Am. Chem. Soc.* **2013**, *135*, 18490–18496, DOI: 10.1021/ja407826d.

(60) Schmeier, T. J.; Dobereiner, G. E.; Crabtree, R. H.; Hazari, N. Secondary Coordination Sphere Interactions Facilitate the Insertion Step in an Iridium(III) CO2 Reduction Catalyst. *J. Am. Chem. Soc.* **2011**, *133*, 9274–9277, DOI: 10.1021/ja2035514.

(61) Ngo, K. T.; McKinnon, M.; Mahanti, B.; Narayanan, R.; Grills, D. C.; Ertem, M. Z.; Rochford, J. Turning on the Protonation-First Pathway for Electrocatalytic CO2 Reduction by Manganese Bipyridyl Tricarbonyl Complexes. *J. Am. Chem. Soc.* **2017**, *139*, 2604–2618, DOI: 10.1021/jacs.6b08776.

(62) DuBois, D. L. Development of Molecular Electrocatalysts for Energy Storage. *Inorg. Chem.* **2014**, *53*, 3935–3960, DOI: 10.1021/ic4026969.

(63) Nichols, E. M.; Derrick, J. S.; Nistanaki, S. K.; Smith, P. T.; Chang, C. J. Positional

effects of second-sphere amide pendants on electrochemical CO2 reduction catalyzed by iron porphyrins. *Chem. Sci.* **2018**, *9*, 2952–2960.

(64) Zee, D.; Nippe, M.; King, A.; Chang, C.; Long, J. R. Tuning Second Coordination Sphere Interactions in Polypyridyl-Iron Complexes to Achieve Selective Electrocatalytic Reduction of Carbon Dioxide to Carbon Monoxide. *Inorg. Chem.* **2020**, just accepted, DOI: `https://doi.org/10.1021/acs.inorgchem.0c00455`.

(65) Shao, Y. et al. Advances in molecular quantum chemistry contained in the Q-Chem 4 program package. *Mol. Phys.* **2015**, *113*, 184–215.

(66) Chai, J.-D.; Head-Gordon, M. Long-range corrected hybrid density functionals with damped atom-atom dispersion corrections. *Phys. Chem. Chem. Phys.* **2008**, *10*, 6615–6620, DOI: `10.1039/B810189B`.

(67) Mardirossian, N.; Head-Gordon, M. ωB97M-V: A combinatorially optimized, range-separated hybrid, meta-GGA density functional with VV10 nonlocal correlation. *J. Chem. Phys.* **2016**, *144*, 214110, DOI: `10.1063/1.4952647`.

(68) Weigend, F.; Ahlrichs, R. Balanced basis sets of split valence, triple zeta valence and quadruple zeta valence quality for H to Rn: Design and assessment of accuracy. *Phys. Chem. Chem. Phys* **2005**, *7*, 3297–3305.

(69) Mardirossian, N.; Head-Gordon, M. Thirty years of density functional theory in computational chemistry: an overview and extensive assessment of 200 density functionals. *Molecular Physics* **2017**, *115*, 2315–2372.

(70) Chan, B.; Gill, P. M.; Kimura, M. Assessment of DFT Methods for Transition Metals with the TMC151 Compilation of Data Sets and Comparison with Accuracies for Main-Group Chemistry. *Journal of chemical theory and computation* **2019**,

(71) Truong, T. N.; Stefanovich, E. V. A new method for incorporating solvent effect into the classical, ab initio molecular orbital and density functional theory frameworks for arbitrary shape cavity. *Chem. Phys. Lett.* **1995**, *240*, 253 – 260, DOI: http://dx.doi.org/10.1016/0009-2614(95)00541-B.

(72) Grimme, S. Semiempirical GGA-type density functional constructed with a long-range dispersion correction. *J. Comput. Chem.* **2006**, *27*, 1787–1799, DOI: 10.1002/jcc.20495.

(73) Becke, A. D. Density-functional exchange-energy approximation with correct asymptotic behavior. *Phys. Rev. A* **1988**, *38*, 3098.

(74) Lee, C.; Yang, W.; Parr, R. G. Development of the Colle-Salvetti correlation-energy formula into a functional of the electron density. *Phys. Rev. B* **1988**, *37*, 785.

(75) Becke, A. D. Density-functional thermochemistry. III. The role of exact exchange. *J. Chem. Phys.* **1993**, *98*, 5648–5652, DOI: http://dx.doi.org/10.1063/1.464913.

(76) Grimme, S.; Antony, J.; Ehrlich, S.; Krieg, H. A consistent and accurate ab initio parametrization of density functional dispersion correction (DFT-D) for the 94 elements H-Pu. *J. Chem. Phys.* **2010**, *132*, –, DOI: http://dx.doi.org/10.1063/1.3382344.

(77) Neese, F. The ORCA program system. *Interdiscip. Rev. Comput. Mol. Sci* **2012**, *2*, 73–78, DOI: 10.1002/wcms.81.

(78) Hellweg, A.; Hättig, C.; Höfener, S.; Klopper, W. Optimized accurate auxiliary basis sets for RI-MP2 and RI-CC2 calculations for the atoms Rb to Rn. *Theor. Chem. Acc* **2007**, *117*, 587–597.

(79) Kelly, C. P.; Cramer, C. J.; Truhlar, D. G. Single-Ion Solvation Free Energies and

the Normal Hydrogen Electrode Potential in Methanol, Acetonitrile, and Dimethyl Sulfoxide. *J. Phys. Chem. B* **2007**, *111*, 408–422, DOI: 10.1021/jp0654031.

(80) Konezny, S. J.; Doherty, M. D.; Luca, O. R.; Crabtree, R. H.; Soloveichik, G. L.; Batista, V. S. Reduction of Systematic Uncertainty in DFT Redox Potentials of Transition-Metal Complexes. *J. Phys. Chem. C* **2012**, *116*, 6349–6356, DOI: 10.1021/jp300485t.

(81) Alongi, K. S.; Shields, G. C. In *Chapter 8 - Theoretical Calculations of Acid Dissociation Constants: A Review Article*; Wheeler, R. A., Ed.; Annual Reports in Computational Chemistry; Elsevier, 2010; Vol. 6; pp 113 – 138, DOI: http://dx.doi.org/10.1016/S1574-1400(10)06008-1.

(82) Liptak, M. D.; Shields, G. C. Accurate pKa Calculations for Carboxylic Acids Using Complete Basis Set and Gaussian-n Models Combined with CPCM Continuum Solvation Methods. *J. Am. Chem. Soc.* **2001**, *123*, 7314–7319, DOI: 10.1021/ja010534f.

(83) Bhattacharjee, A.; Andreiadis, E. S.; Chavarot-Kerlidou, M.; Fontecave, M.; Field, M. J.; Artero, V. A Computational Study of the Mechanism of Hydrogen Evolution by Cobalt(Diimine-Dioxime) Catalysts. *Chem.: Eur. J* **2013**, *19*, 15166–15174, DOI: 10.1002/chem.201301860.

(84) Aktaş, A. H.; Şanlı, N.; Pekcan, G. Spectrometric Determination of pK. *Acta Chim. Slov* **2006**, *53*, 214–218.

(85) Raamat, E.; Kaupmees, K.; Ovsjannikov, G.; Trummal, A.; Kütt, A.; Saame, J.; Koppel, I.; Kaljurand, I.; Lipping, L.; Rodima, T. Acidities of strong neutral Brønsted acids in different media. *Journal of Physical Organic Chemistry* **2013**, *26*, 162–170.

(86) Matsubara, Y. Unified Benchmarking of Electrocatalysts in Noninnocent Second Coordination Spheres for CO2 Reduction. *ACS Energy Letters* **2019**, *4*, 1999–2004.

(87) Fu, Y.; Liu, L.; Yu, H.-Z.; Wang, Y.-M.; Guo, Q.-X. Quantum-Chemical Predictions of Absolute Standard Redox Potentials of Diverse Organic Molecules and Free Radicals in Acetonitrile. *J. Am. Chem. Soc.* **2005**, *127*, 7227–7234, DOI: 10.1021/ja0421856.

(88) Roy, L. E.; Jakubikova, E.; Guthrie, M. G.; Batista, E. R. Calculation of One-Electron Redox Potentials Revisited. Is It Possible to Calculate Accurate Potentials with Density Functional Methods? *J. Phys. Chem. A* **2009**, *113*, 6745–6750, DOI: 10.1021/jp811388w.

(89) Roy, L. E.; Batista, E. R.; Hay, P. J. Theoretical Studies on the Redox Potentials of Fe Dinuclear Complexes as Models for Hydrogenase. *Inorg. Chem.* **2008**, *47*, 9228–9237, DOI: 10.1021/ic800541w.

(90) Canaguier, S.; Fourmond, V.; Perotto, C. U.; Fize, J.; Pecaut, J.; Fontecave, M.; Field, M. J.; Artero, V. Catalytic hydrogen production by a Ni-Ru mimic of NiFe hydrogenases involves a proton-coupled electron transfer step. *Chem. Commun.* **2013**, *49*, 5004–5006, DOI: 10.1039/C3CC40987B.

(91) Salomon, O.; Reiher, M.; Hess, B. A. Assertion and validation of the performance of the B3LYP* functional for the first transition metal row and the G2 test set. *J. Chem. Phys.* **2002**, *117*, 4729–4737, DOI: 10.1063/1.1493179.

(92) Swart, M. Accurate Spin-State Energies for Iron Complexes. *J. Chem. Theory Comput* **2008**, *4*, 2057–2066, DOI: 10.1021/ct800277a.

(93) Ioannidis, E. I.; Kulik, H. J. Towards quantifying the role of exact exchange in predictions of transition metal complex properties. *J. Chem. Phys.* **2015**, *143*, 034104, DOI: 10.1063/1.4926836.

(94) Kepp, K. P. Theoretical Study of Spin Crossover in 30 Iron Complexes. *Inorg. Chem.* **2016**, *55*, 2717–2727, DOI: 10.1021/acs.inorgchem.5b02371.

(95) Droghetti, A.; Alfè, D.; Sanvito, S. Assessment of density functional theory for iron(II) molecules across the spin-crossover transition. *J. Chem. Phys.* **2012**, *137*, 124303, DOI: 10.1063/1.4752411.

(96) Verma, P.; Varga, Z.; Klein, J. E. M. N.; Cramer, C. J.; Que, L.; Truhlar, D. G. Assessment of electronic structure methods for the determination of the ground spin states of Fe(ii), Fe(iii) and Fe(iv) complexes. *Phys. Chem. Chem. Phys.* **2017**, *19*, 13049–13069, DOI: 10.1039/C7CP01263B.

(97) Cometto, C.; Chen, L.; Lo, P.-K.; Guo, Z.; Lau, K.-C.; AnxolabeÌĄheÌĂre-Mallart, E.; Fave, C.; Lau, T.-C.; Robert, M. Highly selective molecular catalysts for the CO2-to-CO electrochemical conversion at very low overpotential. Contrasting Fe vs Co quaterpyridine complexes upon mechanistic studies. *ACS Catalysis* **2018**, *8*, 3411–3417.

(98) Wright, T. C.; Wilkinson, G.; Motevalli, M.; Hursthouse, M. B. (η 2-Acetonitrile) bis (η 5-cyclopentadienyl) molybdenum (II): the first structurally characterized complex containing an η 2-nitrile ligand. *J. Chem. Soc., Dalton Trans.* **1986**, 2017–2019.

(99) Barrera, J.; Sabat, M.; Harman, W. D. Crystal structure of an. eta. 2-acetonitrile complex of tungsten (II): acetonitrile as a four-electron donor. *J. Am. Chem. Soc.* **1991**, *113*, 8178–8180.

(100) Garcia, J. J.; Jones, W. D. Reversible Cleavage of Carbon- Carbon Bonds in Benzonitrile Using Nickel (0). *Organometallics* **2000**, *19*, 5544–5545.

(101) Chetcuti, P. A.; Knobler, C. B.; Hawthorne, M. F. Formation of. eta. 2-side-bonded aryl nitrile complexes from 4-metallaisoxazolin-5-one species and their application in the thermal and photochemical activation of carbon-hydrogen bonds. *Organometallics* **1988**, *7*, 650–660.

(102) Lorente, P.; Carfagna, C.; Etienne, M.; Donnadieu, B. Alkyne and Nitrile as $\eta 2$ (3e) Ligands in [Tris (pyrazolyl) borato] niobium (I) Complexes. Synthesis, Structure, and Coupling Reaction. *Organometallics* **1996**, *15*, 1090–1092.

(103) Butschke, B.; Fillman, K. L.; Bendikov, T.; Shimon, L. J. W.; Diskin-Posner, Y.; Leitus, G.; Gorelsky, S. I.; Neidig, M. L.; Milstein, D. How Innocent are Potentially Redox Non-Innocent Ligands? Electronic Structure and Metal Oxidation States in Iron-PNN Complexes as a Representative Case Study. *Inorg. Chem.* **2015**, *54*, 4909–4926, DOI: 10.1021/acs.inorgchem.5b00509.

(104) Milko, P.; Iron, M. A. On the Innocence of Bipyridine Ligands: How Well Do DFT Functionals Fare for These Challenging Spin Systems? *Journal of chemical theory and computation* **2013**, *10*, 220–235.

(105) Schlimgen, A. W.; Heaps, C. W.; Mazziotti, D. A. Entangled Electrons Foil Synthesis of Elusive Low-Valent Vanadium Oxo Complex. *J. Phys. Chem. Lett* **2016**, *7*, 627–631, DOI: 10.1021/acs.jpclett.5b02547.

(106) Ortuño, M. A.; Cramer, C. J. Multireference Electronic Structures of Fe-Pyridine(diimine) Complexes over Multiple Oxidation States. *J. Phys. Chem. A* **2017**, *121*, 5932–5939, DOI: 10.1021/acs.jpca.7b06032.

(107) Sayfutyarova, E. R.; Sun, Q.; Chan, G. K.-L.; Knizia, G. Automated construction of molecular active spaces from atomic valence orbitals. *J. Chem. Theory Comput* **2017**, *13*, 4063–4078.

(108) Khedkar, A.; Roemelt, M. Active Space Selection Based on Natural Orbital Occupation Numbers From N-Electron Valence Perturbation Theory. *J. Chem. Theory Comput* **2019**,

(109) Stein, C. J.; Reiher, M. Automated selection of active orbital spaces. *J. Chem. Theory Comput* **2016**, *12*, 1760–1771.

(110) Stein, C. J.; Reiher, M. Automated identification of relevant frontier orbitals for chemical compounds and processes. *CHIMIA* **2017**, *71*, 170–176.

(111) Stein, C. J.; Reiher, M. autoCAS: A Program for Fully Automated Multiconfigurational Calculations. *J. Comput. Chem.* **2019**,

(112) Derrick, J.; Loipersberger, M.; Iovan, D.; Smith, P. T.; Chakarawet, K.; Long, J. R.; Head-Gordon, M.; Chang, C. Metal–Ligand Exchange Coupling Promotes Iron-Catalyzed Electrochemical CO2 Reduction at Low Overpotentials. 2020; https://chemrxiv.org/articles/Metal_Ligand_Exchange_Coupling_Promotes_Iron-Catalyzed_Electrochemical_CO2_Reduction_at_Low_Overpotentials/11923176/1.

(113) Vogt, M.; Gargir, M.; Iron, M. A.; Diskin-Posner, Y.; Ben-David, Y.; Milstein, D. A New Mode of Activation of CO2 by Metal-Ligand Cooperation with Reversible C-C and M-O Bond Formation at Ambient Temperature. *Chem.–Eur. J.* **2012**, *18*, 9194–9197, DOI: 10.1002/chem.201201730.

(114) Vogt, M.; Nerush, A.; Diskin-Posner, Y.; Ben-David, Y.; Milstein, D. Reversible CO2 binding triggered by metal-ligand cooperation in a rhenium(i) PNP pincer-type complex and the reaction with dihydrogen. *Chem. Sci.* **2014**, *5*, 2043–2051, DOI: 10.1039/C4SC00130C.

(115) Stichauer, R.; Helmers, A.; Bremer, J.; Rohdenburg, M.; Wark, A.; Lork, E.; Vogt, M. Rhenium(I) Triscarbonyl Complexes with Redox-Active Amino- and Iminopyridine Ligands: Metal-Ligand Cooperation as Trigger for the Reversible Binding of CO2 via a Dearmomatization/Rearomatization Reaction Sequence. *Organometallics* **2017**, *36*, 839–848, DOI: 10.1021/acs.organomet.6b00897.

(116) Flynn, S. R.; Wass, D. F. Transition Metal Frustrated Lewis Pairs. *ACS Catal.* **2013**, *3*, 2574–2581, DOI: 10.1021/cs400754w.

(117) Balaraman, E.; Gunanathan, C.; Zhang, J.; Shimon, L. J. W.; Milstein, D. Efficient hydrogenation of organic carbonates, carbamates and formates indicates alternative routes to methanol based on CO2 and CO. *Nat. Chem.* **2011**, *3*, 609–614.

(118) Sieh, D.; Lacy, D. C.; Peters, J. C.; Kubiak, C. P. Reduction of CO2 by Pyridine Monoimine Molybdenum Carbonyl Complexes: Cooperative Metal-Ligand Binding of CO2. *Chem.–Eur. J.* **2015**, *21*, 8497–8503.

Supporting Information Available

Details on the CASSCF calculations; additional structural information of important intermediates; probe of functional sensitivity using B97-D, B3LYP and ωB97X-D;

Graphical TOC Entry

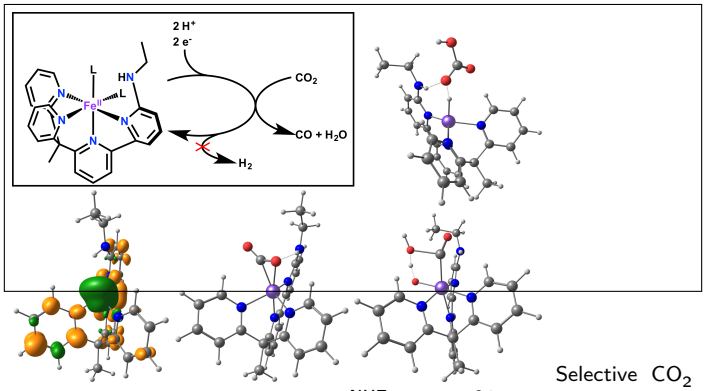

Selective CO_2 reduction reaction using the $[Fe(bpy^{NHEt}PY2)L_2]^{2+}$ (L = H_2O, CH_3CN) catalyst. Spin density of the doubly reduced intermediate (bottom left), CO_2 adduct (bottom middle), transition state for the intramolecular protonation (bottom right) and transition state for hydride formation top.